



HAL
open science

MAVEN Case Studies of Plasma Dynamics in Low-Altitude Crustal Magnetic Field at Mars 1: Dayside Ion Spikes Associated With Radial Crustal Magnetic Fields

Y. I. J. Soobiah, Jared R. Espley, John E. P. Connerney, Jacob R. Gruesbeck,
Gina A. Dibraccio, Jasper Halekas, Laila Andersson, Christopher M. Fowler,
Robert J. Lillis, David L. Mitchell, et al.

► To cite this version:

Y. I. J. Soobiah, Jared R. Espley, John E. P. Connerney, Jacob R. Gruesbeck, Gina A. Dibraccio, et al.. MAVEN Case Studies of Plasma Dynamics in Low-Altitude Crustal Magnetic Field at Mars 1: Dayside Ion Spikes Associated With Radial Crustal Magnetic Fields. *Journal of Geophysical Research Space Physics*, 2019, 124, pp.1239-1261. 10.1029/2018JA025569 . insu-03674458

HAL Id: insu-03674458

<https://insu.hal.science/insu-03674458>

Submitted on 20 May 2022

HAL is a multi-disciplinary open access archive for the deposit and dissemination of scientific research documents, whether they are published or not. The documents may come from teaching and research institutions in France or abroad, or from public or private research centers.

L'archive ouverte pluridisciplinaire **HAL**, est destinée au dépôt et à la diffusion de documents scientifiques de niveau recherche, publiés ou non, émanant des établissements d'enseignement et de recherche français ou étrangers, des laboratoires publics ou privés.

Copyright

RESEARCH ARTICLE

10.1029/2018JA025569

Key Points:

- Investigated plasma transport and associated electrodynamics during ion energy flux spikes in radial crustal fields on the Mars dayside
- Precipitating ion and electron energy flux spikes on closed field consisting of ion beams $E > 1.4$ keV and broad ion distributions $E < 1.4$ keV
- Considered impact of low-altitude precipitating O^+ ions $E > 25$ eV on localized heating and atmospheric escape

Correspondence to:

 Y. I. J. Soobiah,
 yasir.i.soobiah@nasa.gov

Citation:

Soobiah, Y. I. J., Espley, J. R., Connerney, J. E. P., Gruesbeck, J. R., DiBraccio, G. A., Halekas, J., et al. (2019). MAVEN case studies of plasma dynamics in low-altitude crustal magnetic field at Mars 1: Dayside ion spikes associated with radial crustal magnetic fields. *Journal of Geophysical Research: Space Physics*, 124, 1239–1261. <https://doi.org/10.1029/2018JA025569>

Received 11 APR 2018

Accepted 12 SEP 2018

Accepted article online 17 SEP 2018

Published online 1 FEB 2019

MAVEN Case Studies of Plasma Dynamics in Low-Altitude Crustal Magnetic Field at Mars 1: Dayside Ion Spikes Associated With Radial Crustal Magnetic Fields

Y. I. J. Soobiah^{1,2,3} , Jared R. Espley¹ , John E. P. Connerney¹ , Jacob R. Gruesbeck¹ , Gina A. DiBraccio¹ , Jasper Halekas⁴ , Laila Andersson⁵ , Christopher M. Fowler⁵ , Robert J. Lillis⁶ , David L. Mitchell⁶ , Christian Mazelle⁷ , Yuki Harada⁸ , Takuya Hara⁶ , Glyn Collinson^{1,9} , David Brain⁵ , Shaosui Xu⁶ , Shannon M. Curry⁶ , James P. Mcfadden⁶, Mehdi Benna¹ , and Bruce M. Jakosky⁵ 

¹Solar System Exploration Division, NASA Goddard Space Flight Center, Greenbelt, MD, USA, ²Department of Astronomy, University of Maryland, College Park, MD, USA, ³Now at NASA/GSFC, Greenbelt, MD, USA, ⁴Department of Physics and Astronomy, University of Iowa, Iowa City, IA, USA, ⁵Laboratory for Atmospheric and Space Physics (LASP), University of Colorado Boulder, Boulder, CO, USA, ⁶Space Sciences Laboratory (SSL), University of California, Berkeley, CA, USA, ⁷IRAP, University of Toulouse, CNRS, UPS, CNES, Toulouse, France, ⁸Department of Geophysics, Kyoto University, Japan, ⁹Institute for Astrophysics and Computational Sciences, Catholic University of America, Washington, DC, USA

Abstract We report for the first time, simultaneous ion, electron, magnetic field vector and electric field wave measurements made possible by Mars Atmosphere and Volatile Evolution, during ion energy flux spikes in low-altitude radial crustal magnetic fields on the Mars dayside. Observations show energetic electrons and ions ($E > 25$ eV) precipitating on magnetic field lines assumed as closed. Ions ($E < 1.4$ keV) display broad velocity distributions toward Mars, showing ions flowing from higher altitude possibly after magnetic reconnection or loss cone filling from pitch angle scattering effects. Precipitating ions ($E < 1.4$ keV) show nonadiabatic features depending on ion mass and energy and returning ions ($E < 1.4$ keV) show evidence of conserving the first adiabatic invariant in a mirror field. We observe magnetic field perturbations up to 60 nT, electric field wave amplitudes up to 38 mV/m, and brief periods of peaked electron spectra. At ~ 175 km and at times Mars Atmosphere and Volatile Evolution is below the mirroring altitude of electrons, we observe mirroring and transverse heating of H^+ ions alongside increased electric field wave amplitude fluctuations. It suggests field aligned potential drops result from different mirror altitudes of ions and electrons. Ions $E > 1.4$ keV (O^+) occur as injected accelerated ion beams and ions heated after energization or deceleration. Energy dispersed kilo-electron-volt ions suggest a selection effect in radial magnetic fields for lower-energy Marsward ions, compared to reflection of higher-energy anti-Sunward ions. Precipitating kilo-electron-volt ions show energy deposition rates of 3.6×10^{-6} W/m² and sputtering escape rates from precipitating O^+ ions of 1.5×10^5 /(cm².s) and 2.1×10^6 /(cm².s) are calculated.

Plain Language Summary Mars Atmosphere and Volatile Evolution arrived at Mars on 21 September 2014 to study the effects of the solar wind interaction on the upper atmosphere. This study reports the raining of both energetic electrons and multiple populations of ions at low altitudes and over regions of ancient magnetic field from the Martian crust. These observations are associated with large magnetic field deflections and large electric field fluctuations. The results are important for understanding plasma transport and associated electrodynamics where the crustal magnetic fields point vertically toward or away from the planet. Such analysis was not possible with previous missions, which did not include the complete set of space plasma instruments carried by Mars Atmosphere and Volatile Evolution. Some ions display behaviors not expected for the small curvature of the crustal magnetic fields; ions that are locally tied that would require much larger magnetic field structures or ions injected along the direction of the magnetic field. Oxygen ions that originate from Mars that have been picked up by the solar wind and moving at very high speeds are selected over regions of vertical magnetic field to travel directly toward the planet. These ions will have head on impacts with Mars to heat and blast atmosphere out into space.

1. Introduction

Until the arrival of the Mars Atmosphere and Volatile Evolution (MAVEN; Jakosky et al., 2015) mission at Mars on 22 September 2014, it had not been possible to achieve a complete understanding of the plasma transport processes and associated electrodynamic effects in low-altitude (<300 km) regions of the Martian crustal magnetic fields. This is the case since previous Mars missions either did not reach such regions or could not make the simultaneous ion, electron, magnetic field vector, and electric field wave measurements performed by MAVEN's Particle and Fields Package (PFP). Of particular importance to this goal is being able to characterize the kinetic behavior of ions from ion velocity distributions formed with use of in situ vector measurements of the magnetic field, which has not been achieved before in the low-altitude crustal magnetic fields of Mars. Characterizing the behavior of ions is crucial for understanding the plasma dynamics of planetary magnetospheres since ions make the dominant contribution to the transport and loss of mass within a magnetosphere and cases of ion precipitation onto an ionosphere/atmosphere can represent times of large kinetic energy transfer when colliding with the atmosphere (Fang et al., 2013).

As a planet without a strong magnetic field of internal origin, but with a thin tenuous atmosphere, Mars interaction with the solar wind typically follows that of an unmagnetized atmospheric obstacle to the solar wind (Nagy et al., 2004; Vaisberg, 2015). As such the solar wind magnetic field and plasma passing over the Martian obstacle forms an induced magnetosphere through mass loading of the solar wind magnetic field with planetary plasma and the induction of currents and magnetic fields in the Martian ionosphere. An induced magnetosphere involves numerous processes that can energize ions (Dubinin et al., 2011), the most prominent of which include ion pick up from the acceleration of exospheric ions by the solar wind convective electric field (Dubinin, Fraenz, et al., 2006; Yamauchi et al., 2006, 2008; Rahmati et al., 2015), plasma sheet acceleration from the $\mathbf{j} \times \mathbf{B}$ force due to magnetic shear stresses in the magnetotail (Dubinin et al., 1993) and the day-to-night flow of ionospheric plasma associated with the day-to-night pressure gradient (Fränz et al., 2010; Knudsen et al., 1981). Another potential source of energetic ions at Mars is the ionized hot hydrogen and oxygen corona, simulations of which results in O^+ ions with $E > 1$ keV close to Mars (Kallio et al., 2008). The gyroradius of these energetic ion populations can vary between hundreds of kilometers (heavy ions with $E < 1$ keV and protons with $E \sim 1$ keV) to multiples of the Martian radii (heavy ions with $E > 10$ keV) and results in ions that are mostly unmagnetized.

Mars is also host to strong localized crustal sources of magnetic field (Acuña et al., 1998; Connerney et al., 2001, 2005) that are expected to produce local perturbations in the interaction of the solar wind with Mars over the planetary scale, leading to a time and spatial variable obstacle to the solar wind (Brain et al., 2005). The way in which these pockets of strongly magnetized crust modify plasma dynamics of the induced magnetosphere is still poorly understood in terms of in situ particle and fields observations and also how the processes involved, enhance or inhibit atmospheric escape at Mars. Regions of the crustal magnetic field have been observed by previous Mars missions, Mars Global Surveyor (MGS) and Mars Express (MEX), to host magnetic field and particle signatures indicative of different magnetospheric processes that accelerate/energize particles and contribute to the escape of the Martian atmosphere. Signatures of magnetic flux ropes have been identified in a number of different regions around Mars (Briggs et al., 2012). Some magnetic flux rope observations have been related to magnetic reconnection between magnetic fields from the solar wind and crustal magnetic fields (Brain et al., 2010; Hara, Brain, et al., 2017; Soobiah et al., 2014), as well as the detachment of crustal magnetic fields and a bulk escape of the atmospheric plasma of Mars (Brain et al., 2010).

Localized intensifications of electron energy flux, also referred to as electron spikes, that correlate with cusp regions of the crustal magnetic fields have been associated with regions of open magnetic field and the precipitation of magnetosheath electrons toward Mars, made possible by magnetic reconnection between solar wind and crustal magnetic fields (Halekas et al., 2008; Mitchell et al., 2001; Soobiah et al., 2006). This compares to observations on large spatial scales that show a greater probability of lower electron fluxes for regions of higher crustal magnetic field strength (Fränz et al., 2006). Electron spikes and localized enhancements in the peak ionospheric electron density have also been observed in the vicinity of cusps of the crustal magnetic fields on the dayside of Mars as associated with plasma heating from the convection of ionospheric plasma rather than from the precipitation of magnetosheath/solar wind electrons (Nielsen et al., 2007). Here convection of ionospheric plasma, driven by electric fields induced at the interface between the crustal magnetic fields and the solar wind flow, heats the plasma of the low-altitude crustal magnetic field cusps, which can

relate to a reduction in the electron-ion recombination rate that in-turn increases the equilibrium electron density (Nielsen et al., 2007).

Observations of auroral emission in regions of the Martian crustal magnetic field (Bertaux et al., 2005) are indicative of processes taking place at Mars that are analogous to the auroral processes of plasma acceleration and energization at Earth (Lundin et al., 2006). Indeed, this is supported by the strong correlation of crustal magnetic field regions with observations in the high altitude nightside of Mars of “inverted-V” electron and ion energy-time structures showing the acceleration of electrons toward Mars and the acceleration of ions away from Mars (G erard et al., 2015; Lundin, Winningham, Barabash, Frahm, Holmstr om, et al., 2006). Moreover, peaked electron energy distributions have been observed on the circular mapping orbits of MGS at 400 km altitude to correlate with regions most likely to involve open magnetic field on the nightside of Mars (Brain et al., 2006). Such examples of accelerated electrons are considered as evidence for the auroral acceleration in a quasi-static electric potential drop at Mars (Brain et al., 2006; Lundin, Winningham, Barabash, Frahm, Holmstr om, et al., 2006; Lundin, Winningham, Barabash, Frahm, Brain, et al., 2006). In addition, at the times of peaked electron distributions, MGS also observed perturbations in the magnetic field indicative of a deflection in the magnetic field from field aligned currents (Brain et al., 2006; Halekas et al., 2008). Also, calculations using MGS premapping orbit data show enhanced Hall conductivity in regions of crustal magnetic fields between 100 and 250 km and greater likelihood of perpendicular currents being supported in these regions (Opgenoorth et al., 2010). Such properties are typical of auroral phenomena and solar wind ionosphere coupling at Earth that support the presence of parallel electric fields and potential drops. The theory of such structures at Earth has been shown to also be applicable to Mars (Dubinin et al., 2008). Furthermore, recent analysis of MGS electron pitch angle data has shown evidence of field-aligned electrostatic potentials in the Martian ionosphere, which possibly form due to electric currents associated with solar wind ionosphere coupling in regions of crustal magnetic field (Lillis et al., 2018). The particle precipitation and associated field aligned electric fields related to nightside aurora or dayside coupling between the solar wind and the Martian ionosphere has the potential to affect the dynamics of the Martian ionosphere and the neutral atmosphere, leading to an outflow of ions (Ergun et al., 2006).

While previous observations at Mars have been able to characterize in detail the properties of electron and magnetic field signatures in regions of the crustal magnetic field, a similar level of detail in the properties of ion signatures and their relation to the plasma dynamics of the Martian crustal magnetic fields is still limited. Previous studies by MEX have shown a poor one to one correlation between electron precipitation signatures and corresponding ion signatures, where the general low energy/cold component of heavy-ions flowing away from Mars remain mostly unchanged (Soobiah et al., 2013). This was considered the result of the finite gyroradius effect from the large gyroradius of heavy ions in regions of crustal magnetic field. Cases of precipitating energetic electrons in crustal magnetic field cusps have been associated with the auroral-like outflow of planetary ions (Dubinin et al., 2009), as well as the simultaneous presence of cold ionospheric ions and a more energetic component of heated ions (Dubinin et al., 2011).

Statistical studies using MEX data have shown how crustal magnetic field regions can effect ion dynamics to either inhibit ion escape rates (Lundin et al., 2011; Nilsson et al., 2011) or result in enhanced escape rates for pre-terminator locations between 60°–80° solar zenith angles (SZA) (Ramstad et al., 2016). Modeling of the solar wind interaction with Mars arrive at similar results where ion escape rates are shown to respond to the presence of crustal magnetic fields, where the crustal fields can act as a protective shield deflecting the solar wind around the Martian atmosphere (Dong et al., 2015; Fang et al., 2010) or when placed close to dawn or dusk local times cause increased escape rates (Ma et al., 2014; Fang et al., 2015). Furthermore, regions of crustal magnetic field may drive the precipitation of pick-up ions toward the atmosphere of Mars, leading to an increase in energy deposition and also sputtering (Curry et al., 2015; Li et al., 2011), a process thought to be important in the escape of the Martian atmosphere (Leblanc & Johnson, 2001, 2002).

In this paper, using data from the MAVEN spacecraft, we examine for the first time at Mars the kinetic properties of ion transport and the associated plasma dynamics observed during broad energy range spikes of ion energy flux in low-altitude regions of radial crustal magnetic field on the dayside of Mars. The case studies reported here include the first observations made in the low-altitude crustal magnetic field regions of Mars of rare and extraordinary ion energy-time structures made up of ion spikes that extend to kilo-electron-volt energies when coinciding with energy dispersed structures of kilo-electron-volt ions that develop into energy-time structures of kilo-electron-volt ion bands. This work also accompanies the companion study by

Hara et al. (2018) showing statistical evidence for the crustal magnetic field control of precipitating ion fluxes observed by MAVEN into the upper atmosphere of Mars.

2. Data Set

This study presents data from the PFP suite of instruments on MAVEN. The Solar Wind Ion Analyzer (SWIA; Halekas, Taylor, et al., 2015) and the SupraThermal And Thermal Ion Composition (STATIC; McFadden et al., 2015) provides measurements of ion energy distributions, with STATIC providing ion mass information. The Solar Wind Electron Analyzer (SWEA; Mitchell et al., 2016) provides measurements of the electron energy distributions at high time cadence of 2 s. Note that units of energy flux or “EFlux” presented here using SWIA, STATIC, and SWEA data correspond to units of $\text{eV}/(\text{cm}^2 \cdot \text{s} \cdot \text{sr} \cdot \text{eV})$. The MAGnetic field investigation (MAG; Connerney, Espley, Lawton, et al., 2015; Connerney, Espley, DiBraccio, et al., 2015) provides three-dimensional magnetic field measurements with a maximum cadence of 32 vector samples per second. The MAG vector is presented in the planetocentric reference frame where positive B_ϕ is the component of magnetic field directed Eastward, positive B_θ is the component of magnetic field directed Southward and positive B_r is the component of magnetic field directed radially away from the planet. The Langmuir Probe and Waves (LPW) instrument (Andersson et al., 2015) is used to provide single component electric field measurements from DC to ~ 2 MHz.

3. The Coincidence of Broad Energy Range Ion Spikes and Kilo-Electron-Volt Ion Band Features in Low-Altitude Radial Crustal Magnetic Field

3.1. MAVEN Observations From 26 October 2015

Figure 1 shows MAVEN PFP data from orbit 2088 on 26 October 2015 as MAVEN moved outbound from periaresis over a region of strong crustal magnetic field, revealing extraordinary ion energy-time structures in low-altitude (>300 km) crustal magnetic fields on the dayside of Mars. That is the localized broad energy range spikes in ion energy flux in regions of radial crustal magnetic field that also coincide with the energy dispersion of kilo-electron-volt ions and a energy-time kilo-electron-volt ion band feature. Between times of 10:47:20 UT to 10:47:32 UT and 10:50:44 UT to 10:51:00 UT SWIA observes prominent spikes in ion energy flux over a broad range in energy, between 25 eV and ~ 1 keV and highlighted by additional cyan ovals. The ion spikes, referred to hereafter as ion spikes 1 and 2, occur as temporally and spatially confined structures in regions of increased radial magnetic field and coincide with a change in sign of one of the horizontal components of magnetic field.

As observed by SWIA is a band of ions in the energy-time spectrogram between 1.4 and 10 keV and 10:50:00 UT and 10:54:28 UT. Close to ion spike 2 between 10:51:0 UT and 10:51:52 UT, ions from the kilo-electron-volt ion band are observed below 4 keV and to increase in energy such that between 10:51:52 UT and 10:54:28 UT the kilo-electron-volt ion band is observed between 4 and 10 keV. STATIC observations (cf. Figures 1b–1d) show the kilo-electron-volt ion band is formed of O^+ ions. The origin of such ions are unknown, but similar observations of kilo-electron-volt ions from the induced magnetosphere of Mars have been associated with O^+ ions picked up by the solar wind that are precipitating toward Mars in the -E hemisphere (Hara, Luhmann, et al., 2017). A more detailed investigation of the properties of this kilo-electron-volt ions band feature is left for future work.

STATIC observations (cf. Figures 1b–1d) show ion spikes 1 and 2 composed of multiple ion populations, O^+ and O_2^+ ions from 25 eV to 0.1 keV characteristic of planetary ions, H^+ ions from 0.1 to ~ 1 keV characteristic of the magnetosheath ions. Ion spike 2 also includes O^+ ions with energies >1 keV, characteristic of the O^+ ions picked up by the solar wind. Beyond 10:54:00 UT as the altitude of MAVEN increases and strength of the crustal magnetic field decreases, there is an extended region of ions between 25 eV and 10 keV with low energy flux showing a similar make up of ions observed during ion spikes 1 and 2.

Figures 1f and 1g shows during ion spikes 1 and 2, lower and medium energy ion populations are characterized by distributions of ions that are broad and asymmetric with a greater energy flux of ions observed in the hemisphere directed towards Mars. Figure 1e shows the higher energy ion population during ion spikes 1 and 2 have ion energy distributions are far narrower in angular range that is more field aligned and directed toward Mars compared to the lower and medium energy ion populations.

SWEA measures a slight enhancement in the energy flux of electrons at energies >60 eV (cf. Figure 1h) neighboring ion spike 2, between 10:51:03 UT and 10:51:05 UT, referred to hereafter as electron spike A (labeled to

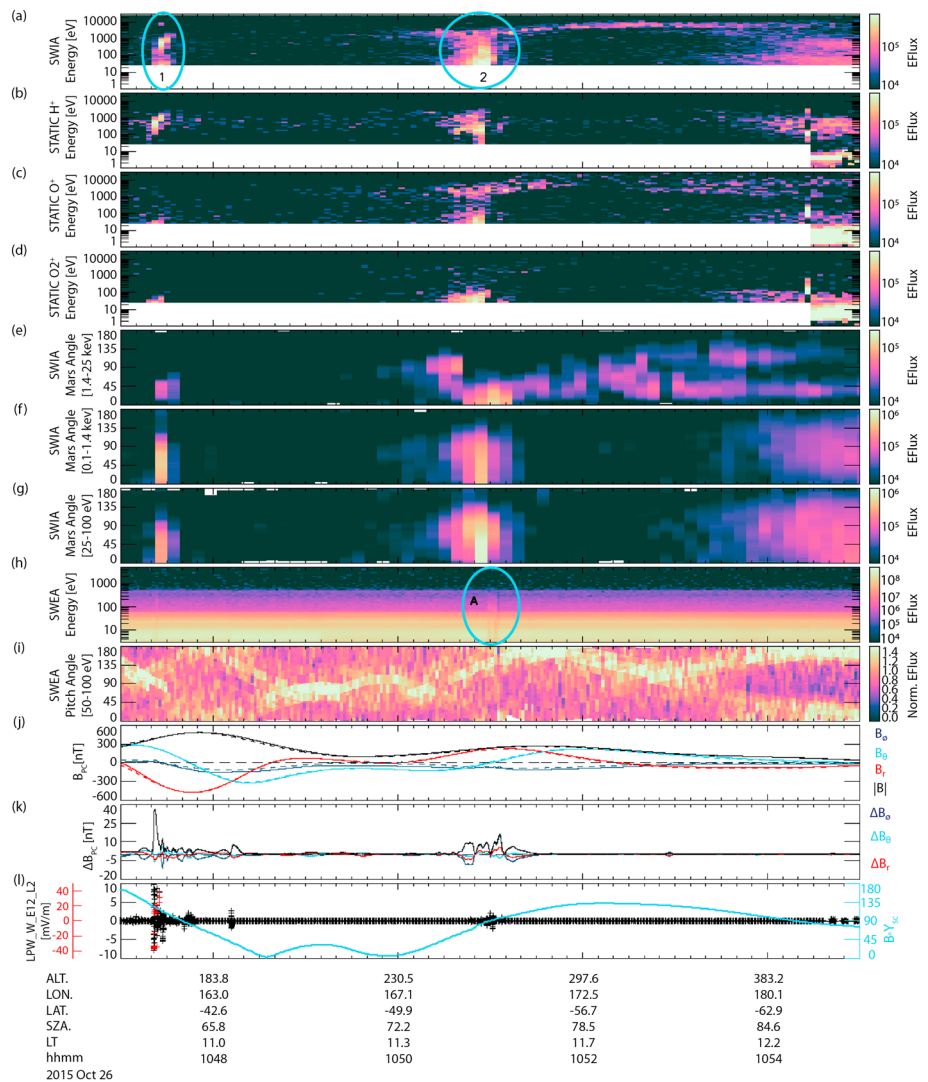


Figure 1. MAVEN observations orbit 2088 on 26 October 2015, showing broad energy range ion spikes and kilo-electron-volt ion bands at altitude <300 km. (a) SWIA omnidirectional ion energy flux energy-time spectrogram, (b)–(d) STATIC H^+ , O^+ and O_2^+ omnidirectional ion energy flux energy-time spectrogram, (e)–(g) SWIA ion angular distribution functions between 1.4–25 keV, 0.1–1.4 keV, and 25 eV to 0.1 keV (0° directed toward Mars), (h) SWEA omnidirectional electron energy flux energy-time spectrogram, (i) SWEA electron pitch angle distribution between 50 and 100 eV (j) MAG magnetic field vectors in planetocentric coordinates, eastward (dark blue), southward (light blue), radial (red), and magnitude (black) compared to the Morschhauser et al. (2014) crustal magnetic field model (dotted lines respectively), (k) MAG magnetic field perturbations from background magnetic field in planetocentric coordinates and magnitude of perturbation (black), (l) LPW electric field wave amplitude below 10 mV/m (black) and above 10 mV/m (red) and angle between the spacecraft frame Y-axis and the local magnetic field (light blue). Horizontal axis labels show spacecraft altitude, longitude, latitude, solar zenith angle, local time, and universal time, respectively. SWIA = Solar Wind Ion Analyzer; SWEA = Solar Wind Electron Analyzer; MAG = MAGnetic field investigation; LPW = Langmuir Probe and Waves; STATIC = SupraThermal And Thermal Ion Composition.

the left of the electron spike and highlighted by an additional cyan oval). Figure 1i shows the modest electron spike has electron pitch angles that are mostly antiparallel to the magnetic field and directed toward Mars. Throughout most of the time period of Figure 1, including the duration of ion spikes 1 and 2 and electron spike A, field aligned photoelectrons are observed directed both toward and away from Mars (not shown). The topology of magnetic field related to such observations is discussed in section 4.

Figure 1k shows how both ion spikes 1 and 2 coincide with periods of large perturbations in the magnetic field vectors from the background magnetic field, with the perturbation in the magnetic field showing typical magnitudes of ± 10 nT. Note that an approximate background magnetic field is obtained by the addition of the

background magnetic field from Mars, assumed as that from the Morschhauser et al. (2014) crustal magnetic field model, and a background magnetic field from external sources. The background magnetic field from external sources is determined by subtracting the Morschhauser et al. (2014) crustal magnetic field model from the MAG measured magnetic field and then using a low-pass filter with a 0.5 Hz (20 s) cutoff frequency on the difference. This method leads to a more desirable midline fit across magnetic field perturbations for the variety of cases investigated here as compared to the removal of a low-pass filter with a 0.5 Hz (20 s) cutoff frequency of the total magnetic field alone.

The black axis and data points of Figure 11 shows how both ion spikes 1 and 2 coincide with periods of increased electric field wave amplitude, with typical values around ± 2 mV/m. Note that the electric field wave amplitude has been obtained using a sliding window average of the raw electric field data taken from spectra of plasma wave electric field recorded during LPW's passive and active modes (see Andersson et al., 2015, for details on LPW operation). Figure 11 has also accounted for low-frequency noise from LPW as described in Fowler et al. (2017). Near the onset of ion spike 1, around 10:47:21 UT, there are large outliers for both the magnetic field perturbation of ~ 36 nT and electric field wave amplitude that fluctuates between ± 40 mV/m as shown by the red axis and symbols. These large electric fields were observed with a stable background electric field and did not result from the sudden change in the background electric field typified when crossing sharp plasma boundaries (Fowler et al., 2017). In order to determine an electric field, the LPW booms are separated by 12.68 m in the direction parallel to the Y-axis of the MAVEN spacecraft frame. The angle of this direction from the local magnetic field is given by the light blue line in Figure 11 with the accompanying axis to the right of the panel. This shows during the times of ion spikes 1 and 2, the increased electric field wave amplitude measured by LPW corresponds to electric fields perpendicular or oblique to the magnetic field.

3.2. MAVEN Observations From 2 June 2015

Figure 2 shows MAVEN PFP data from orbit 1307 on 2 June 2015 as MAVEN passed periapsis over a region of strong to moderate crustal magnetic field. As with observations presented in Figure 1a from orbit 2088 of MAVEN, Figure 2a shows SWIA observes spikes in ion energy flux between 25 eV and ~ 1 keV between times of 06:08:42 UT and 06:08:59 UT, 06:10:58 UT and 06:11:18 UT, 06:13:18 UT and 06:14:02 UT, and 06:14:50 UT and 06:15:46 UT and highlighted by additional cyan ovals. The ion spikes, referred to hereafter as ion spikes 3, 4, 5, and 6, are temporally and spatially confined to regions of increased strength in the radial magnetic field and coincide with a change in sign of one of the horizontal components of magnetic field.

For completeness STATIC data are included in Figures 2b and 2c and show STATIC measurements affected by background noise as well as a change in the operating mode of the instrument. Prior to 06:11:36 UT and adjacent to periapsis, STATIC is in conic mode and measures ions between 0.1 and 500 eV. After 06:11:42 UT and during periapsis, STATIC is in ram mode and measures ions between 0.1 and 50 eV (McFadden et al., 2015). Note, between 06:08:30 UT and 06:08:54 UT, STATIC is able to distinguish an energization of O_2^+ ions during ion spike 3 (cf. Figure 2d).

Figure 2a shows a band of ions between energies 5 and 14 keV observed by SWIA between 06:09:30 UT and 06:13:31 UT. This is comparable to the ion band feature presented in Figure 1a and also displays a cutoff in time with the appearance of ion spike 5. The similarity in appearance and energies of this ion band feature to that observed in Figures 1a and 1c would suggest the ion band feature of Figure 2a is the result of O^+ ions. An additional band of ions observed between 0.7 and 1.4 keV (peaking at ~ 1 keV) follows features identified as penetrating solar wind H^+ ions in the Martian ionosphere (Halekas, Lillis, et al., 2015).

Figure 2f and 2g show that the lower-energy ion population during ion spikes 3 and 4 and the lower- and medium-energy ion populations during ion spikes 5 and 6 are characterized by broad energy distributions that are asymmetric with greater energy flux of ions directed toward Mars. During ion spikes 4, 5, and 6, there is also an appreciable component of ions moving away from Mars. Figure 2e shows the higher energy ion population during ion spike 5 displays an increase in the field aligned component of ions directed toward Mars. Whereas the high-energy ion distributions in surrounding regions are dominated by ions moving anti-Sunward (broad angular distribution at larger angles to Mars).

Accompanying ion spikes 3, 5, and 6, between 06:08:33 UT and 06:08:59 UT, 06:13:21 UT and 06:13:35 UT, 06:14:55 UT and 06:15:01 UT, and 06:15:19 UT and 06:15:29 UT, SWEA measures appreciable spikes in the energy flux of electrons over a few hundreds of electron volts as highlighted by additional cyan ovals

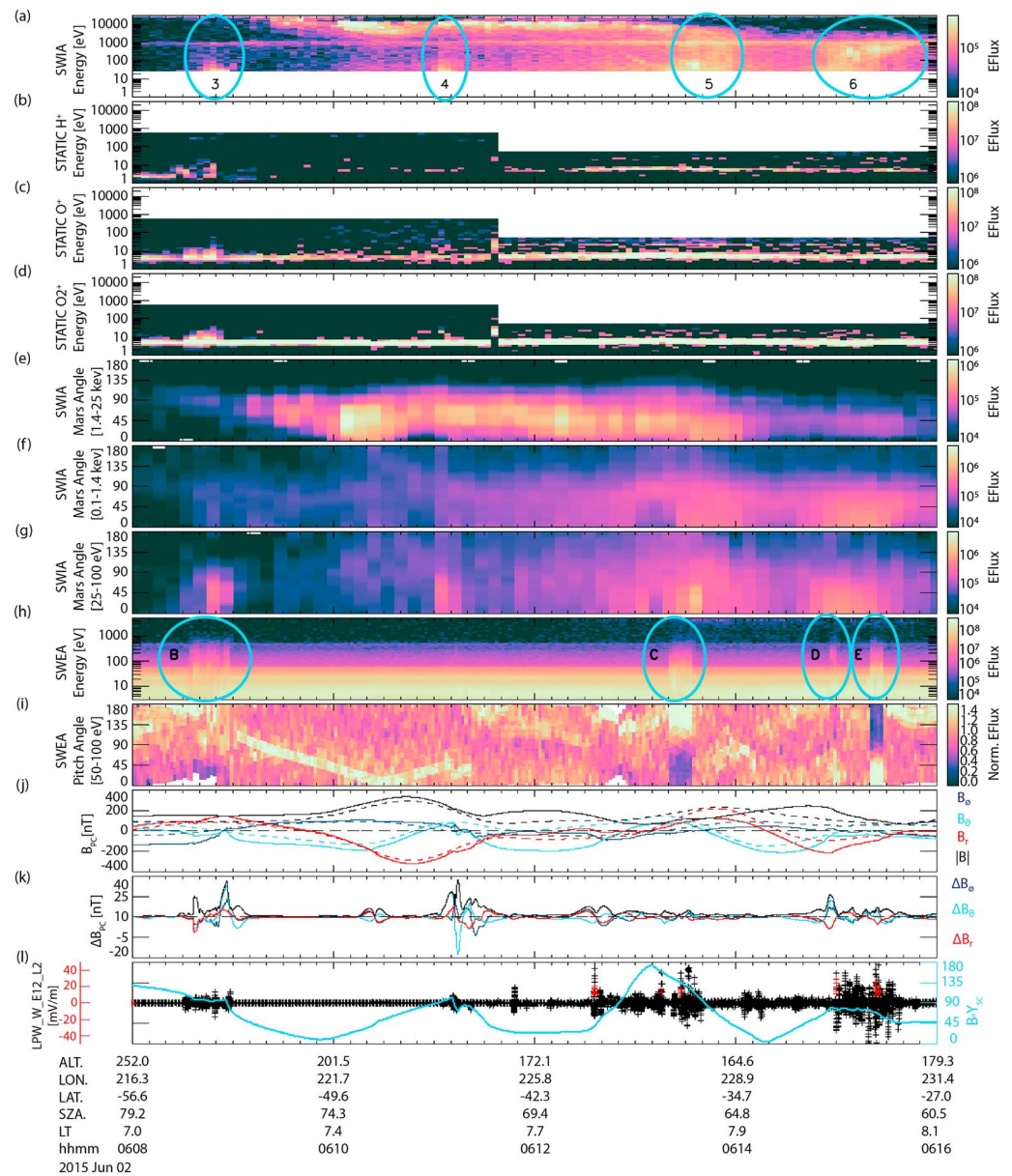


Figure 2. MAVEN observations from orbit 1307 on 2 June 2015, showing signatures of broad energy range ion spikes and kilo-electron-volt ion bands at altitude <300 km. Figure format identical to Figure 1. MAVEN = Mars Atmosphere and Volatile EvolutionN.

(cf. Figure 2h). The electron spikes from Figure 2h are referred to hereafter as electron spikes B, C, D, and E electron spikes (as labeled to the left of each electron spike).

Figure 2i shows the pitch angle distributions of the electron spikes are formed of field aligned electrons directed toward Mars. Note that electron spikes B, C, and E occur with a sharp drop off in the normalized energy flux in the hemisphere directed away from Mars, at angles from around 60° for electron spike B and from around 90° for electron spikes C and E, respectively.

At the time of the ion spikes, Figures 2k and 2l show perturbations in the magnetic field vectors from the background magnetic field, typically around ± 10 nT in magnitude, as well as increased electric field wave amplitude, varying between ± 2 mV/m (black axis and data points) and ± 20 mV/m (red axis and data points). Note that ion spikes 3 and 4 occur with large deflections in magnetic field of up to 60 nT magnitude. As part of the electric field wave amplitude measured by LPW, but not shown are outliers of ~ 70 mV/m at 06:11:47 UT, ~ 63 mV/m at 06:12:07 UT, and ~ 100 mV/m at 06:15:00 UT, associated with sudden changes in the background

electric field typified when crossing sharp plasma boundaries (Fowler et al., 2017). As in the previous case, the angle the Y -axis of the MAVEN spacecraft frame makes with the local magnetic field (light blue line and axis) shows that during the times of ion spikes 3 to 6, the increased electric field wave amplitude measured by LPW corresponds to electric fields perpendicular or oblique to the magnetic field.

4. Electron Spikes in Low-Altitude Radial Crustal Magnetic Field That Are Open or Closed

Different methods are available to derive magnetic field topology at Mars from electron measurements using electron pitch angle distributions (Brain et al., 2007) or pitch angle resolved electron energy spectra (Xu et al., 2017). For the former method, regions of closed magnetic field are identified by two-sided loss cones (trapped distributions—both dayside and nightside), fully isotropic distributions (dayside) and plasma void distributions (nightside). Open magnetic field are identified in regions of strong crustal magnetic field where the field-aligned electrons returning from the planet is much reduced compared to other pitch angles, that is one-sided loss cones (Brain et al., 2007). The type of electron energy spectra measured serves as an indication of the connection a magnetic field line has with certain regions of plasma. For example closed magnetic fields will have both ends of the magnetic field connected to the source region of the ionosphere and would show photoelectrons traveling in both directions along the magnetic field (Xu et al., 2017). Open magnetic field lines would have one end connected to the source region of the ionosphere and one end connected to the solar wind/magnetosheath and would show photoelectrons traveling away from Mars and solar wind/magnetosheath electrons traveling toward Mars (Xu et al., 2017). Draped magnetic field lines would have both ends connected the solar wind/magnetosheath and would show solar wind/magnetosheath electrons traveling in both directions along the magnetic field (Dubinin et al., 1994; Xu et al., 2017).

Electron loss cones indicative of open magnetic field topology are observed in cases of electron spike A for energies >70 eV (not shown) and electron spike B as shown by the average electron pitch angle distribution between 50 and 100 eV (cf. Figure 2i). Note that, for energies <70 eV, electron spike A has a more bidirectional electron distribution with field aligned electrons traveling both toward and away from Mars. Both electron spikes A and B are observed with photoelectrons that are both parallel and antiparallel to the magnetic field. While electron spikes A and B are observed above 200 km, electron spikes C, D, and E are observed below 200 km. At these times pitch angles distributions lack a loss cone since there is a sharp drop in normalized energy flux of electrons from pitch angles of 90° . Such a feature is indicative of the spacecraft being below the mirroring altitude of electrons. That is, there is lack of electrons being reflected to form a loss cone before being absorbed by the atmosphere below the spacecraft.

Figure 3 shows a diverse range of electron pitch angle resolved energy spectra measured during electron spikes B, C, D, and E. Note that the spectra have not been corrected for spacecraft potential, which has been derived from SWEA and LPW as between -0.5 and -3 V for times 06:08:00 UT to 06:13:07 UT and 06:13:29 UT to 06:16:00 UT (Figures 3a and 3b and 3e–3h) and between -3 and -4 V for times 06:13:07 UT to 06:13:29 UT (Figures 3c and 3d). It is assumed the distinct peaks in energy flux measured on field-aligned directions both toward and away from Mars during the electron spikes close to photoelectron energies, 21 to 24 eV (solid vertical line) and 27 eV (dashed vertical line), are due to photoelectrons produced by photoionization of carbon dioxide and atomic oxygen (Frahm et al., 2006). For electron spikes A, B, C, D, and E, 23 SWEA 2-s electron energy spectra include coverage of field aligned directions toward and away from Mars. Of these 23 electron energy spectra, 21 were measured with photoelectron peaks in the energy spectra of field aligned electrons traveling toward and away from Mars.

The results described above show magnetic field topology is ambiguous for the cases of dayside electron spikes A to E presented here. Observations support both magnetic field being open where loss cones are observed (electron spikes A and B) and precipitating solar wind/magnetosheath-like electrons are observed (electron spikes B to E) and magnetic field being closed where bidirectional electron pitch angle distributions are observed (electron spike A) and photoelectron peaks observed in both directions along the magnetic field (electron spikes A to E). In order to simplify the discussions that follow we assume electrons spikes A to E occur on closed magnetic fields and that observations of photoelectrons showing closed magnetic field take precedence over conflicting features in support of open magnetic field. The electron energy spectra from Figures 3e–3h measured during electron spike D and E show, in addition to the peak in photoelectrons, there are peaks in energy flux of more energetic electrons measured around 150 and 50 eV, respectively. These

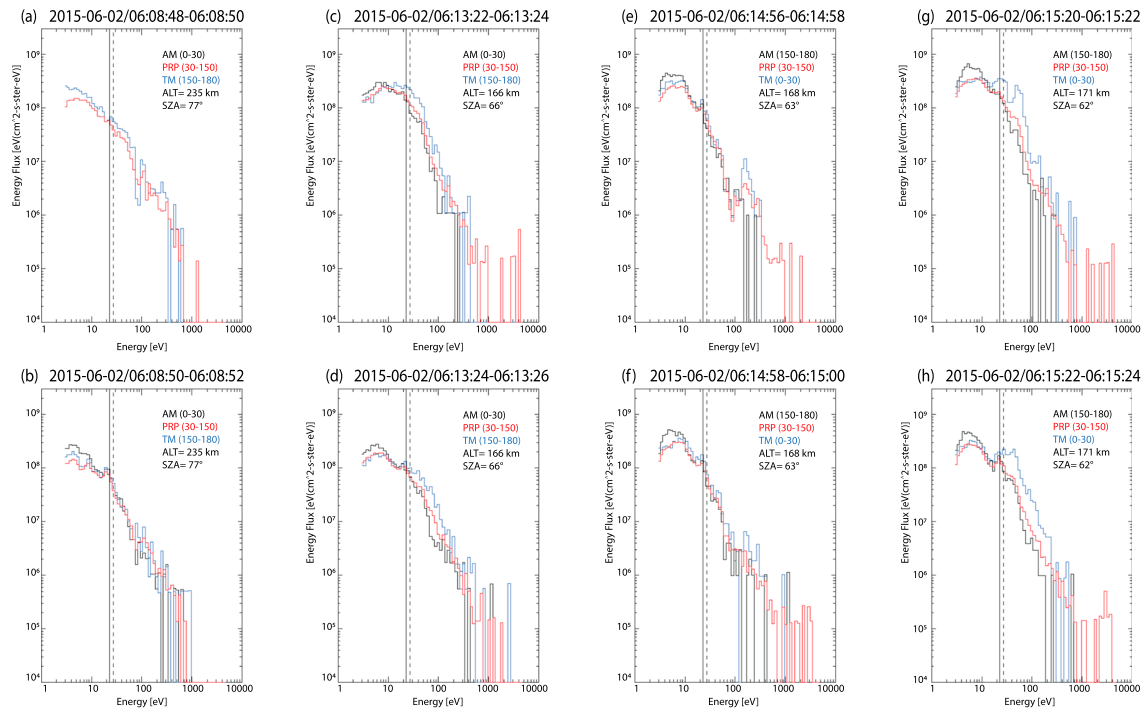


Figure 3. Pairs of consecutive 2-s SWEA electron energy spectra showing evidence of closed magnetic field topology and diverse energy spectra during electron spikes B, C, D, and E, as well as brief periods of accelerated electrons during electron spikes D and E from orbit 1307 on 2 June 2015 (cf. Figure 2h). Electron energy spectra are plotted for field-aligned directions that are most toward Mars in blue (TM), most away from Mars in black (AM) and perpendicular to the magnetic field in red. Vertical lines are also plotted at the CO₂ and O ionization energies around 23 and 27 eV (solid and dashed lines, respectively) to help identify photoelectron peaks in each spectra. SWEA electron energy spectra have not been corrected for spacecraft potential, which is estimated to be between -0.5 and -3 V for Figures 3a and 3b and $3e-3h$ and between -3 and -4 V for Figures 3c and 3d. SWEA = Solar Wind Electron Analyzer.

observations allow for a number of different interpretations. Typically, peaks in electron energy flux at higher energies are indicative of the acceleration of electrons through field aligned potential drop (Brain et al., 2006), which in the case presented here would occur over very brief periods and possibly relate to LPW measurements of strong wave amplitude electric fields on short time scales. The observations alongside photoelectron peaks could indicate the presence of a field aligned potential drop on closed or open magnetic field, where ionospheric electrons traveling away from Mars are reflected by the potential drop to form peaks in photoelectrons traveling toward Mars (Collinson et al., 2015). Another interpretation is the injection of energetic electrons on closed magnetic fields on the Martian dayside (Harada et al., 2016).

5. Characteristics of Energetic Ions in Low-Altitude Closed Radial Crustal Magnetic Field on the Dayside of Mars

Figure 4 considers how regions of crustal magnetic field with different magnetic field strengths may cause different energetic ion populations from the induced magnetosphere to precipitate toward Mars. Figure 4a presents a color graph of ion gyroradius as a function of perpendicular energy and magnetic field strength with different color scale axes for H⁺, O⁺, and O₂⁺, respectively. Highlighted are the perpendicular energies of H⁺ (1.2 keV), O⁺ (80 eV) and O₂⁺ (40 eV) that results in a gyroradius of 100 km in a 50 nT magnetic field.

In scenario 1 from Figure 4b, the gyroradius of ions are sufficiently large compared to the spatial scale of the crustal magnetic fields such that ions are unmagnetized and the magnetic moment of the particle is not conserved as an invariant of motion. Under such conditions, ions that encounter crustal magnetic fields at large pitch angles may penetrate to very low altitudes before being magnetically reflected. Ions that encounter crustal magnetic fields with smaller pitch angles will have less perpendicular energy and be more magnetized and as a result may be deflected into the foot points of the crustal magnetic field in regions of radial magnetic field. Ions that encounter radial crustal magnetic fields on Marsward/field aligned trajectories will precipitate toward the foot points. This scenario is analogous to the deflection of solar wind ions by Lunar magnetic anomalies forming regions of enhanced ion density or halos, at the foot points of the magnetic field

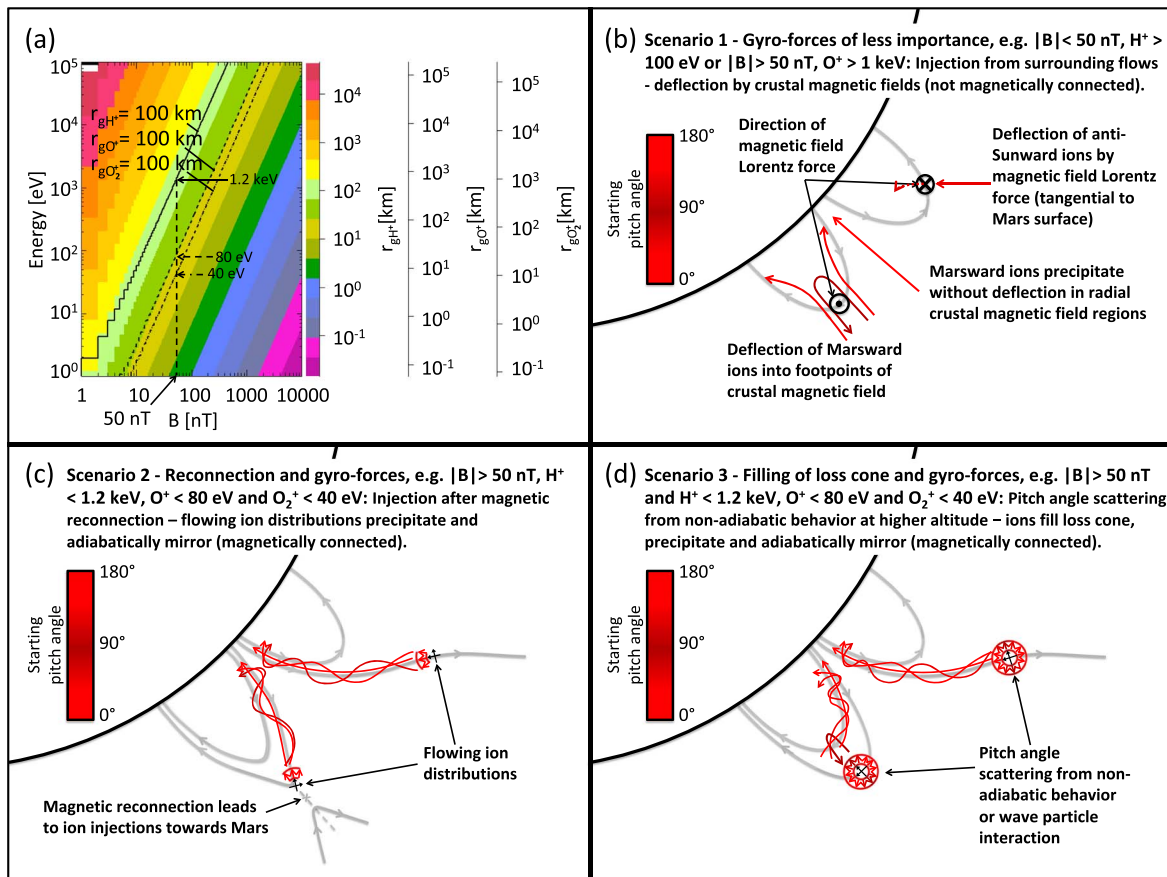


Figure 4. Effects of ion gyroradius on the interaction of ions moving toward the Martian crustal magnetic fields. (a) Color graph of ion gyroradius as function of perpendicular energy and magnetic field strength with different color scale axes for H^+ , O^+ and O_2^+ , respectively. (b) Scenario 1—finite gyroradius effects of H^+ ions $E > 100$ eV moving toward regions of weak crustal magnetic fields or O^+ ions $E > 1$ keV moving toward both weak or strong crustal magnetic fields. (c) Scenario 2—precipitation of field aligned flows of different ion populations due to magnetic reconnection. (d) Scenario 3—precipitation of field aligned flows of different ion populations due to filling of the ion loss cone.

(Kallio et al., 2012). Note, in the case of the Lunar magnetic anomalies, observations show evidence of strong electric fields in regions of remnant magnetic fields (Futaana et al., 2013; Saito et al., 2012) that are also reproduced in models of the solar wind interaction and would contribute to the deflection of ions by the Lorentz force into foot points of the magnetic field. In this type of interaction, the ion velocity distributions observed above the altitudes where magnetic reflection occurs should be highly asymmetric with respect to the radial direction. That is, beams of ions move toward and beams of reflected ions move away from the magnetic anomalies (Deca et al., 2015).

In scenarios 2 and 3 from Figures 4c and 4d, respectively, ions precipitating in low-altitude regions of the radial crustal magnetic field are shown to have a magnetic connection to higher altitudes on either closed or open magnetic field. Ions at higher altitude with small enough pitch angles will flow along the magnetic field. This can result due to magnetic reconnection as shown in Figure 4c or due to the filling of the loss cone as shown in Figure 4d. The latter may occur in the presence of pitch angle scattering effects, which could occur when the gyroradius of ions are of similar scale to the crustal magnetic fields or from some wave particle interaction. In both cases shown by Figures 4c and 4d, ions that initially have small enough pitch angles may be sufficiently magnetized to conserve the first adiabatic invariant to mirror and reflect at higher altitudes as compared to the unmagnetized ions presented in scenario 2. Particles with this property are adiabatic and as such should satisfy the so-called parameter of adiabaticity being much greater than one (Grigorenko et al., 2009). The parameter of adiabaticity, κ , was introduced by Buchner and Zelenyi (1986) and is defined as the square root of the ratio of the minimum radius of curvature of the magnetic field, R_{cmin} , to the maximum gyroradius of a particle, r_{gmax} , $\kappa = \sqrt{(R_{cmin}/r_{gmax})}$. For $\kappa < 1$, particles may adhere to a quasi-adiabatic motion

(Buchner & Zelenyi, 1989), whereas values of κ approaching unity describe particles that may experience nonadiabatic dynamics that are subject to chaotic motion and particle scattering. Note, in the example of Figure 1j, there is 12° of latitude that separates the maximum radial magnetic field measured at 10:47:45 UT and 10:51:06 respectively, which is equivalent to a radius of curvature of around 370 km at an altitude of 180 km and a κ of around 2 for $r_{gmax} = 100$ km. Therefore, the adiabatic behavior of energetic ions is not to be expected for regions of crustal magnetic fields observed here. Rather, pitch angle scattering effects may be expected.

Note that the possibility for adiabatic behavior in low-altitude crustal magnetic field regions will be counteracted as ion-neutral collisional frequency increases as altitude or SZA decreases. That is, when the ion gyrofrequency to ion-neutral collisional frequency is equal to or less than unity ions are considered unmagnetized. Unfortunately, neutral density measurements from the MAVEN Neutral Gas and Ion Mass Spectrometer (NGIMS; Mahaffy, Benna, King, et al., 2015) were not available for time periods considered here. However, in sections 5.1 and 5.2 we estimate the ratio of ion gyrofrequency to ion-neutral collisional frequency using an updated version of Figure 4 from Mahaffy, Benna, Elrod, et al. (2015) of the distribution of the average CO_2 neutral density measured by NGIMS as a function of SZA and altitude using 13 months of data from November, 2015 to end of December, 2016.

The following discussion investigates the 3-D field of view (FOV) ion distributions and 2-D ion velocity distributions during ion spikes 2 and 5 and ion spikes 1 and 6, respectively. The 3-D FOV ion distributions have been centered on Mars and the 2-D ion velocity distributions have been organized with respect to the magnetic field direction such that parallel velocities are plotted along the horizontal axis. The 2-D ion velocity distribution interpolates and smooths over data points gathered in a $\pm 20^\circ$ polar angular range about the magnetic field direction. The plane of the 2-D ion velocity used is that which best resolves the parallel ion beam and is not oriented with respect to the direction of the local convective electric field. Both 3-D FOV and 2-D ion velocity distributions have been corrected for spacecraft velocity. The 3-D FOV and 2-D ion velocity distributions are not corrected for spacecraft potential or bulk velocity. We do not expect the inclusion of a spacecraft potential of a few volts and a bulk velocity dominated by the cold ion population below 10 eV (not measured by STATIC) to produce any significant difference for velocity distributions of ions measured above 25 eV.

5.1. Precipitating 25-eV to 1.4-keV Flowing-Ion and Kilo-Electron-Volt Ion-Beam Distributions

Figure 5 compares SWIA 3-D FOV ion distributions and SWIA 2-D ion velocity distributions between 10:50:52 UT and 10:50:56 UT, 26 October 2015 and during ion spike 2. Figure 6 compares SWIA 3-D FOV ion distributions and SWIA 2-D ion velocity distributions during ion spike 5 and between 06:13:42 UT and 06:13:46 UT, 2 June 2015. The figures show ion distributions from three energy ranges 1.4–25 keV, 0.1–1.4 keV, and 25 eV to 0.1 keV. The different energy ranges have been chosen to reflect the different ion populations identified by STATIC during ion spikes 1 and 2 (cf. Figures 1b–1d).

Figures 5a and 5b show that during ion spike 2, ions $E > 1.4$ keV associated with O^+ ions, are characterized by a clear narrow antiparallel beam of ions directed toward Mars. This is indicative of ions accelerated externally that have been injected into the local region. Whereas during ion spike 5, Figures 6a and 6b show ions $E > 1.4$ keV are characterized by a distribution of field aligned ions directed toward Mars, which extends between velocities corresponding to energies of 0.3–4.5 keV. This is indicative of a local heating process, but it is unknown if this is a result of a local energization or deceleration process. Examples of the latter are observed in cases of deceleration of solar wind ions at the Lunar magnetic anomalies (Saito et al., 2012).

In terms of ions $E > 1.4$ keV associated with O^+ ions, the distinct beams of accelerated and heated ions precipitating toward Mars are indicative of the type of interaction presented by Figure 4b, where the ion gyro-forces are less important. Further aspects of this precipitation is discussed in sections 6 and 7.

Figures 5c–5f show ions associated with H^+ ions between 0.1 and 1.4 keV and ions associated with O^+ and O_2^+ between 25 eV to 0.1 keV are characterized by an asymmetrical distribution where larger phase space densities are observed alongside a broad velocity distribution in the antiparallel hemisphere directed toward Mars. This feature is also reproduced during ion spike 5 as shown in Figures 6c–6f. Figure 5d shows ions associated with H^+ ions between 0.1 and 1.4 keV occur with distinctly different distributions above and below a velocity of 250 km/s (320 eV). Below 250 km/s the ion velocity distribution shows higher phase space density and is more isotropic in the antiparallel direction, whereas above 250 km/s the distribution is more structured and fragmented. Figure 5f shows ions between 25 eV to 0.1 keV as associated with O^+ and O_2^+ ions, displaying

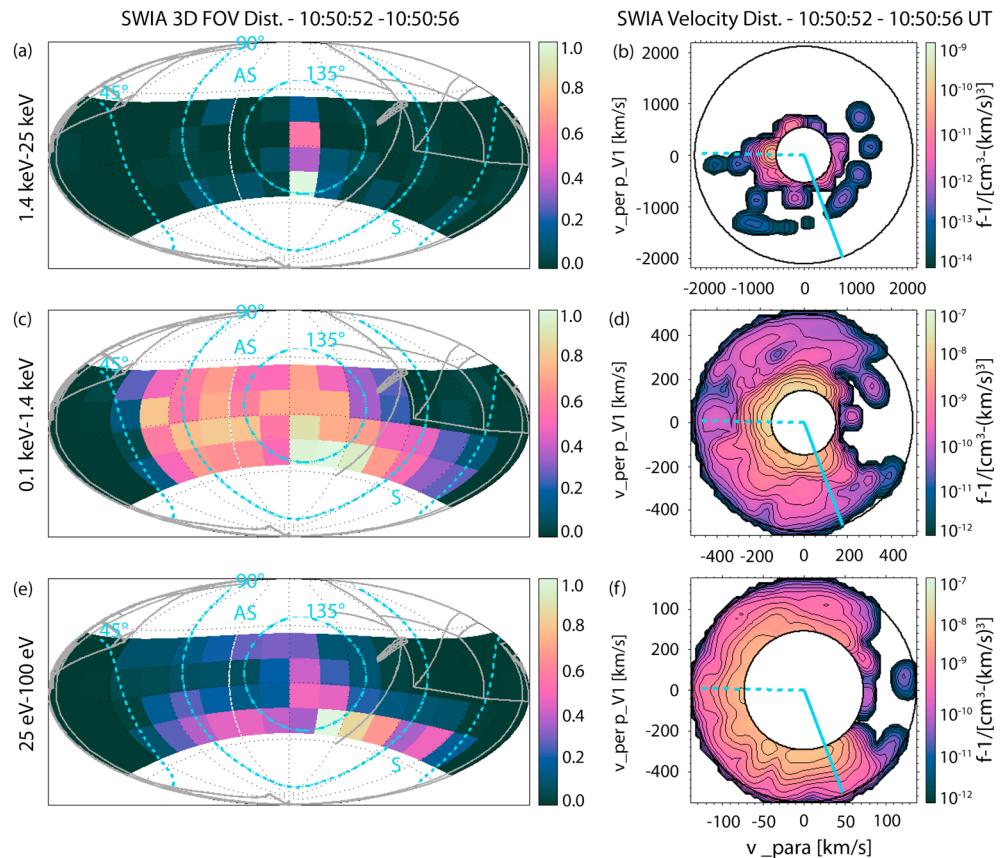


Figure 5. Comparison of SWIA 3-D field of view (FOV) ion distributions (left-hand column of panels) and SWIA 2-D ion velocity distributions (right-hand columns of panels) over three energy ranges 1.4 keV - 25 keV (top row), 0.1 keV - 1.4 keV (middle row) and 25 eV - 0.1 keV (bottom row) between 10:50:52 UT and 10:50:56 UT, 26 October 2015 and during ion spike 2. Note, during this period the magnetic field is mostly radial with elevation angles of 68° – 72° . SWIA 3-D FOV ion distributions are centered on Mars and include labels for Sunward (S) and anti-Sunward (AS) directions, as well as light blue contours to show angles of 45° , 90° , and 135° from the magnetic field direction. A grey outline is used to illustrate the MAVEN spacecraft in the instrument FOV. Right-hand column of panels show the SWIA 2-D ion velocity distributions in a plane consisting of velocity parallel to the magnetic field along the horizontal axis and velocity perpendicular to the magnetic field along the vertical axis. Solid and dashed light blue lines show directions toward the Sun and Mars respectively. SWIA 2-D ion velocity distributions axes show velocities for H^+ ions (the velocity of O^+ and O_2^+ ions may be obtained by dividing values on axes by 4 and 5.65, respectively). SWIA = Solar Wind Ion Analyzer; MAVEN = Mars Atmosphere and Volatile EvolutionN.

a similar fragmented structure to the distribution above 250 km/s from Figure 5d. A fragmented structure observed in ion velocity distributions is indicative of nonadiabatic effects and have been modeled by Martin et al. (2000) as well as observed by Vaisberg et al. (2015) in regions of the Earth magnetosphere where nonadiabatic effects are important.

In comparison, Figure 6d and 6f shows that during ion spike 5, the antiparallel distribution of ions precipitating toward Mars is generally less structured. However, there is a more appreciable component of ions directed away from Mars. This includes narrow components of enhanced phase space density aligned along the Sunward direction over a wide range of velocity and beams of ions at lower velocity that are oblique to the magnetic field direction and directed away from Mars (cf. Figures 6d and 6f). Note that Figure 6e shows a distinct beam of ions in the anti-Sunward direction that most likely correspond to penetrating solar wind protons.

In terms of ions $E < 1.4$ keV, the similar broad ion velocity distribution for ions between 0.1–1.4 keV and 25 eV to 0.1 keV, would suggest the ion populations between these energy ranges have been transported from similar regions at higher altitudes with some magnetic connection between regions of crustal magnetic field at higher altitudes and radial magnetic field foot points at lower altitude. This would indicate the type

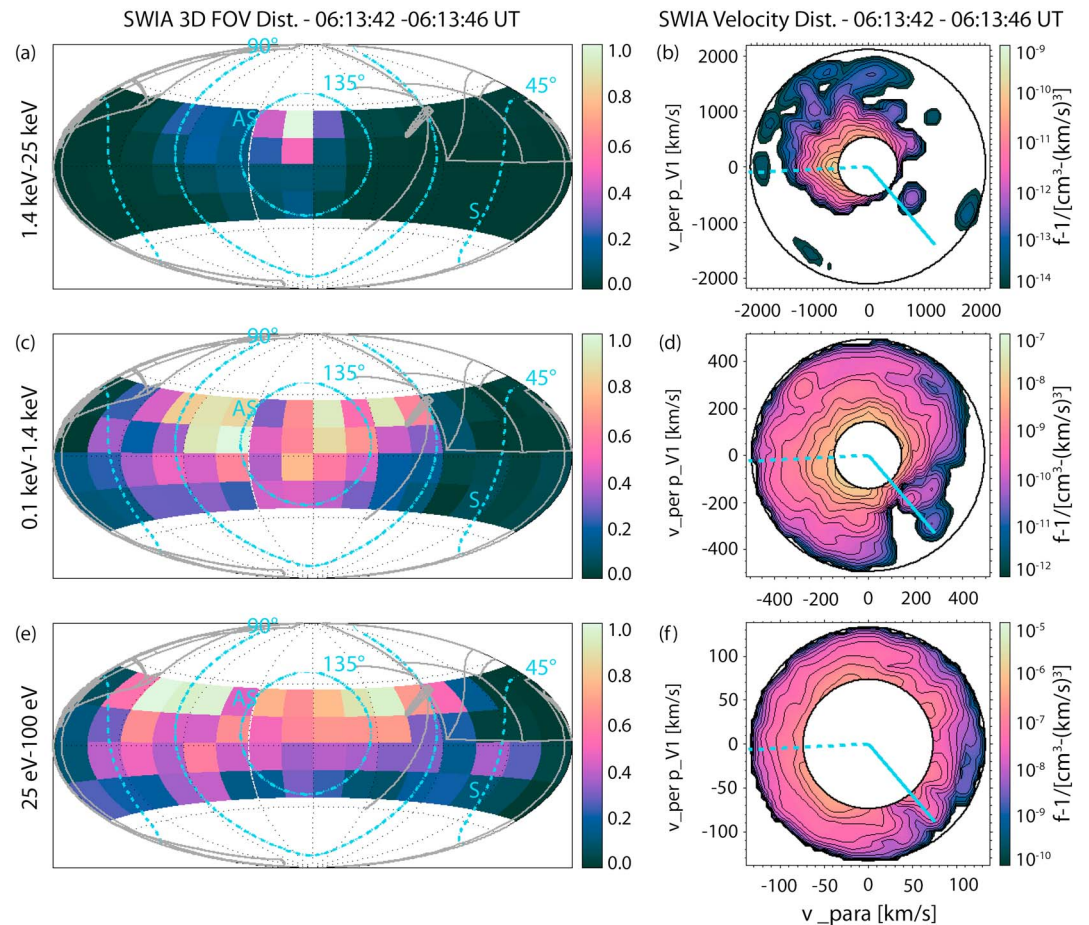


Figure 6. Comparison of SWIA 3-D FOV ion distributions (left-hand column of panels) and SWIA 2-D ion velocity distributions (right-hand columns of panels) over three energy ranges 1.4–25 keV (top row), 0.1–1.4 keV (middle row), and 25 eV to 0.1 keV (bottom row) between 06:13:42 UT and 06:13:46 UT, 2 June 2015 and during ion spike 5. During this time MAVEN is situated in a region of radial crustal magnetic field with local elevation angle of 74°–85°. Format of 3-D FOV ion distributions and 2-D ion velocity distributions follows that from Figure 5. SWIA = Solar Wind Ion Analyzer; MAVEN = Mars Atmosphere and Volatile Evolution; FOV = field of view.

of interaction presented by Figures 4c and 4d, where the ion gyro-forces are of greater importance. This is supported by the observations of a reflected component of ions directed away from Mars (cf. Figures 4c–4f and 6c–6f). Indeed, Figure 5c–5f shows in the case of ion spike 2, in the parallel hemisphere directed away from Mars, is a sharp drop in phase space density for an approximately constant angle about the parallel axis over both, 25 eV to 0.1 keV and 0.1–1.4 keV, energy ranges. Such a feature is indicative of an ion loss cone and supports a conservation of the first adiabatic invariant and also raises the prospects of ions being absorbed by the Martian atmosphere. That is losing energy through collisions, contributing to the sputtering process and also possibly resulting in auroral emissions. However, the parameter of adiabaticity does not support adiabatic effects during the time of Figure 5a and 5b. If assuming a magnetic field radius of curvature of 370 km and considering magnetically reflected H^+ ions between 0.1 and 1.4 keV and O^+ and O_2^+ ions between 25 eV and 0.1 keV, results in values of κ ranging from 3 to 8.

In the case of Figures 5d and 5f, evidence of magnetic mirroring is observed around 260 km at a time STATIC data is available to identify different ion species. Using NIGMS 2015 average data, the ratio of ion gyrofrequency to ion-neutral collision frequency is much greater than unity at this altitude and SZA and remains greater than unity down to altitudes of 147.5 km or lower for H^+ , 152.5 km for O^+ and 162.5 km for O_2^+ . However, a loss cone of 45° at a measured magnetic field strength of around 220 nT gives a mirroring field strength of around 450 nT, which corresponds to an altitude of around 150 km if using the Morschhauser et al. (2014)

model. Therefore, it seems plausible as long as the parameter of adiabaticity is sufficiently large, the observed populations of O^+ with $E > 25$ eV and H^+ with $E > 0.1$ keV will remain magnetized down to the mirror altitude.

In the case of Figures 6d and 6f, Figure 6d does not show any obvious loss cone, although there is an appreciable reflected component that is asymmetrical about the parallel axis. Figure 6f shows a more defined loss cone that is symmetrical about the parallel axis at around 57° pitch angle. At lower pitch angles and within the loss cone, there are ions moving away from Mars in a conic-like distribution that is symmetrical about the parallel axis and is suggestive of ions being mirrored up the field line. Using NIGMS 2015 average data, the ratio of ion gyrofrequency to ion-neutral collision frequency is greater than unity at this altitude and SZA and remains greater than unity down to altitudes of 147.5 km or lower for H^+ , whereas the ratio is less than unity for O^+ and O_2^+ at the altitude at observation. Therefore, O^+ and O_2^+ are expected to be unmagnetized at this time and would not be expected to result in the evidence of magnetic mirroring in Figure 6f. Instead, such features may result from the presence of H^+ ions between 25 eV and 0.1 keV, but are not possible to identify due to the lack of STATIC measurements at this time. Also, as the observed magnetic field ($|B| \sim 130$ nT) is much perturbed compared to the Morschhauser et al. (2014) model ($|B| \sim 230$ nT) it is not possible to determine if a population H^+ ions are magnetized down to the mirroring altitude at this time.

The precipitation of ions and electrons in regions of radial magnetic field where ions show signs of conserving the first adiabatic invariant lends itself to the comparison of similar features observed in the dayside cusp region at the Earth, where open reconnected magnetic field leads to the precipitation of electrons and ions and the mirroring of ions (Bouhram et al., 2002; Onsager et al., 1993). Similar ion velocity distributions are also observed at Mercury showing flowing ion distributions of magnetosheath plasma precipitating in the cusp regions (Raines et al., 2014). Moreover, models of the solar wind interaction with Mars have also shown how magnetosheath plasma may flow along open field lines to become focused in cusps of the Martian crustal magnetic fields (Brecht & Ledvina, 2012).

However, given the interpretation of SWEA electron measurements showing closed magnetic field during the ion spikes reported here, the ion velocity distributions presented here are interpreted as ions flowing along closed magnetic field lines from higher altitude crustal magnetic field. This is supported by the energy-mass composition of ions associated with ion spikes 1 and 2 also being observed above ~ 390 km during the same periapsis pass and in a region of more horizontal crustal magnetic field (after 10:54:00 UT in Figure 1a–1d). Figure 4c presents one possible explanation involving the reconnection of once open crustal magnetic fields forming closed magnetic field and Marsward flows of ions (Harada et al., 2015).

Figure 4d presents another possible explanation involving the filling in of the ion loss cone. The later may occur from the pitch angle scattering and isotropization of flows of ions from the induced magnetosphere that have drifted on to crustal magnetic fields. A similar case has been successfully modeled to explain ion precipitation on closed magnetic field of the dayside polar region of the Earth magnetosphere (Alem & Delcourt, 1995). Unfortunately, without further observations or simulations, it is difficult to differentiate between ions that are precipitating as a result of magnetic reconnection or ions precipitating as a result of the filling of the loss cone. In any case, further study of ion spikes in regions of radial crustal magnetic field could prove an important tool for the remote sensing of processes related to magnetic reconnection or nonadiabatic effects of crustal magnetic fields.

Depending on the energy of the ions the interaction with the Martian crustal magnetic fields has properties in common with Lunar type interaction presented in Figure 4b and scenario 1, where precipitating ions above 1.4 keV are beam like. However, below 1.4 keV the ion interaction seems quite unlike the Lunar example and instead points to greater magnetization above the mirroring altitude and reflects the type of interaction presented in Figures 4c and 4d and scenarios 2 and 3.

5.2. Downward Mirroring Ions and Upward Ion Conics

Figure 7 shows SWIA 3-D FOV and 2-D ion velocity distributions associated with H^+ ions between 0.1 and 1.4 keV during ion spikes 1 and 6. Both ion spikes 1 and 6 show field aligned distributions of ions with a high phase space density spread over a wide range of parallel velocity precipitating toward Mars (cf. Figures 7b and 7d). The SWEA 3-D FOV and 2-D electron velocity distributions during electron spike E is also shown to highlight the remarkable similarity in the 3-D FOV of SWIA and SWEA during ion spike 6 showing the simultaneous field aligned precipitation of ions and electrons toward Mars (cf. Figures 7e and 7f).

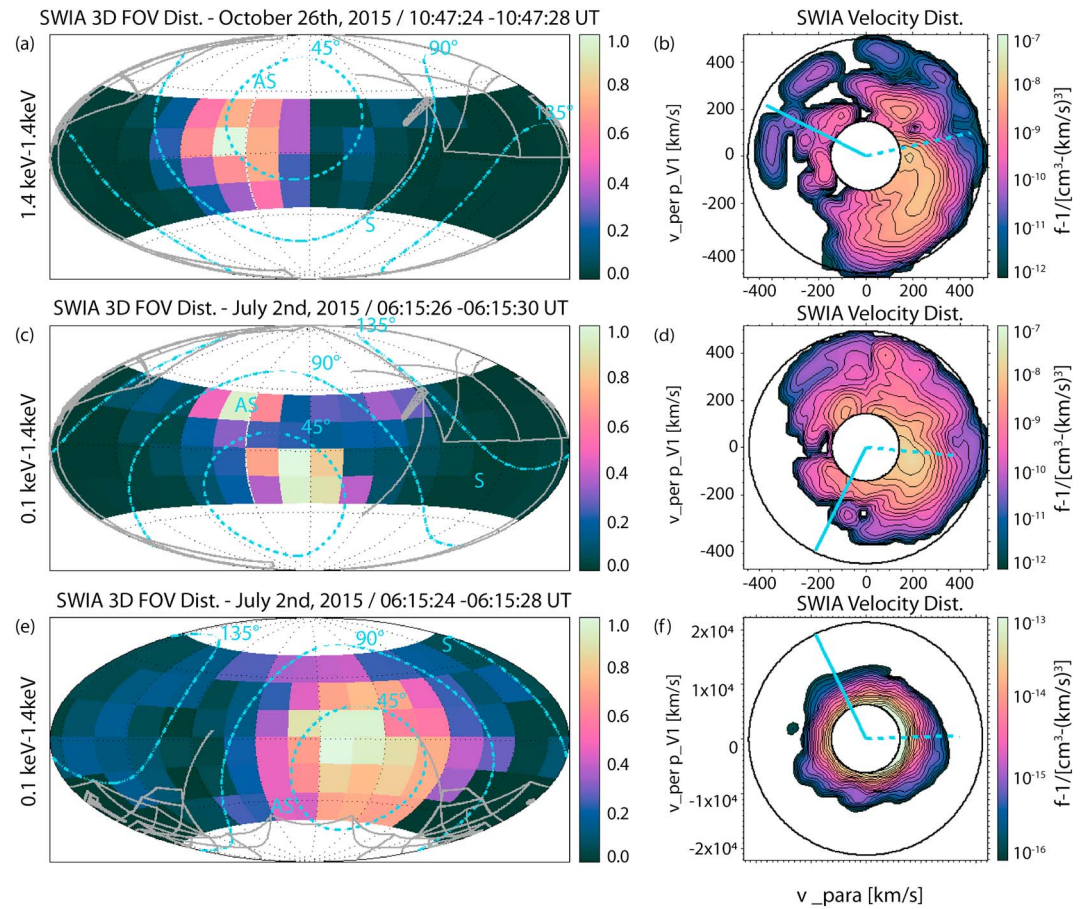


Figure 7. SWIA and SWEA 3-D FOV ion and electron distributions (left-hand column of panels) and 2-D ion and electron velocity distributions (right-hand columns of panels) between the energy range 0.1 and 1.4 keV showing the conservation of the first adiabatic invariant by ions in a magnetic field mirror field. (a–b) SWIA ion distributions obtained during ion spike 1 and between 10:47:24 UT and 10:47:28 UT on 26 October 2015. During this time the magnetic field elevation angle varies between -63° and -55° . (c–d) SWIA ion distributions obtained during ion spike 6 and between 06:15:26 UT and 06:15:30 UT, 2 June 2015. During this time the magnetic field elevation angle varies between -58° and -40° . (e–f) SWEA electron distributions during electron spike E and between 06:15:26 UT and 06:15:28 UT. During this time the magnetic field elevation angle varies between -58° and -48° . Format of 3-D FOV ion and electron distributions and 2-D ion and electron velocity distributions follow that from Figure 5. FOV = field of view; SWIA = Solar Wind Ion Analyzer; SWEA = Solar Wind Electron Analyzer.

During ion spikes 1 and 6, but most pronounced during ion spike 1 (cf. Figure 7b), the ion velocity distributions show departure from field-aligned angles for increasing parallel velocity leading to a broad distribution that is asymmetrical about the parallel direction. The distribution of larger ion phase space density extends out to larger pitch angles along the negative perpendicular axis for increasing parallel velocity. Also in both cases of ion spikes 1 and 6, the observed characteristics described in the parallel hemisphere are reproduced for ion velocity distributions over nearly 90° polar angle revolution around the parallel direction (not shown). Combined with an asymmetry in the perpendicular direction, the velocity distribution of the precipitating ions of Figures 7b and 7d represents a nongyrotropic partial ion ring distribution about the magnetic field. Ion ring velocity distributions observed for downflowing ions in the magnetic field cusp region of the Earth are considered to demonstrate the conservation of the first adiabatic invariant in a converging mirror field (Gorney, 1983). Therefore, the above observation of a partial ion ring distribution would be the first evidence of a similar process in the crustal magnetic fields of Mars.

The observation of ion mirroring for the energy range associated with H^+ ions in regions of the radial crustal magnetic field of Mars is an important part of understanding the dynamics of the Martian radial crustal magnetic field/cusps. First, it illustrates further how energetic ions (H^+ ions) are at least partially magnetized in regions of crustal magnetic field despite the parameter of adiabaticity not supporting adiabatic effects during

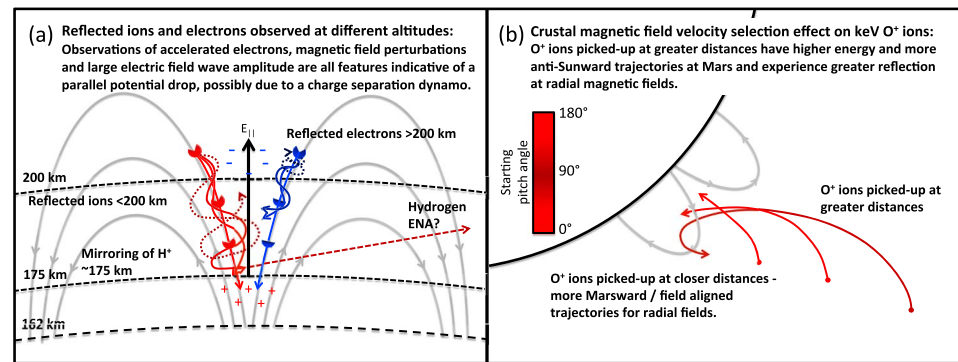


Figure 8. Schematics summarizing (a) how the different altitudes where reflected electrons and ions occur may lead to formation of a charge separation dynamo and parallel electric field potential drop as well as the production of ENA hydrogen from the mirroring of H⁺ ions (b) velocity selection effect of keV O⁺ ions in regions of low-altitude radial crustal magnetic field. Note that particle trajectories with darker shades represent particles that have a larger pitch angle when initially interacting with the Martian crustal magnetic fields.

these time periods. For example, assuming a 370-km magnetic field radius of curvature and H⁺ ions observed as mirroring mostly below 830 eV, κ is around 6 during the time of Figures 7a and 7b and is around 3 during the time of Figure 7c and 7d. The adiabatic behavior observed in the ion velocity distributions presented here and in section 5.1 is contrary to the expected lack of adiabatic behavior from the radius of curvature of the crustal magnetic field currently being considered. This would suggest different ions populations are injected onto crustal magnetic fields with mostly field aligned distributions and have low enough perpendicular velocity to ensure some adiabatic behavior. Alternatively, the radius of curvature of the crustal magnetic field that has been considered could be significantly underestimated at a few hundred kilometers.

Second, the observation of electrons and different ion species mirroring at different altitudes in the crustal magnetic field cusps raises the prospect of a charge separation dynamo and associated parallel electric fields forming in these regions. However, in the regions of radial crustal magnetic field and periods of ion spikes presented here, LPW's single axis measurements did not provide coverage along the magnetic field and measured large electric field wave amplitudes at perpendicular to oblique angles to the magnetic field. Ion spike 1 and 6 for which mirroring ions are observed, occur at 175 km and 173 km respectively. This compares to electron spike B observed with a loss cone and above 200 km and electron spike C, D, and E observed without a strong mirroring of electrons or a loss cone at 164, 169, and 173 km, respectively. Figure 8a summarizes such observations and shows how the difference in altitudes where energetic electrons (blue arrows, negative symbols and energy distributions) and H⁺ ions (red arrows, positive symbols and energy distributions) in regions of radial crustal magnetic field may lead to some amount of charge separation, allowing a charge separation dynamo and associated parallel electric fields to form (represented by black arrow and E_{||}). Such a process would also support the presence of large wave amplitude electric fields as measured by LPW and also field aligned currents as related to the large magnetic field perturbations measured by MAG.

Third, the nongyrotropic partial ion ring distributions observed as part of the mirroring H⁺ ion velocity distributions could be unstable to plasma wave instabilities resulting in the energization of ions in analogy to similar velocity distributions observed in the dayside cusp region at Earth (Cattell & Hudson, 1982; Roth & Hudson, 1985; Hudson & Roth, 1986). Indeed, the ion velocity distribution presented from ion spike 6 shows the simultaneous observation of downflowing ions and upflowing ions, which occur at quite conical pitch angles about the magnetic field and indicate a transverse ion energization and ion outflow process similar to that observed for the Earth cusp (Øieroset et al., 1999, and references therein).

Fourth, while the observations of precipitating heavy ions may result in atmospheric escape from energy deposition and sputtering, mirroring H⁺ ions in low-altitude radial crustal magnetic field may also aid atmospheric escape from Mars through the charge exchange process. As shown in Figure 8a a mirroring H⁺ ion may charge exchange with the background neutral atmosphere forming an energetic neutral hydrogen atom that is able to escape from Mars. This would be analogous to similar processes thought to occur at Earth (Roelof, 1997). This could also explain MEX observations showing an enhancement of hydrogen ENA flux in the presence of crustal magnetic fields on the dayside of Mars (Wang et al., 2014). The formation of an hydrogen ENA

in the above process would potentially lead to the escape of this hydrogen from Mars. Therefore, ignoring the effects of sputtering caused by the precipitating H^+ ions, which is marginal compared to that caused by the precipitation heavier ions such as the planetary O^+ ions, the escaping ENA formed by the charge exchange process on the precipitating H^+ ions could represent an additional escape of planetary hydrogen from Mars if the original source of the precipitating H^+ ions is from the hot ion corona of Mars instead of the solar wind.

This study also presents the first such measurements at Mars by MAVEN's LPW, of large fluctuating large electric field wave amplitudes in regions of radial crustal magnetic field and during observations of ion spikes. Although LPW lacks coverage in the direction aligned with the magnetic fields during these periods, the fluctuations of electric fields perpendicular to the magnetic field could also involve oppositely directed electric fields that are adjacent to each other as related to possible small scale double layer structures and associated parallel electric fields (Block, 1988). Unfortunately, as LPW is unable to determine the vector direction of the DC electric field and therefore also an accurate baseline electric field, it is not possible to determine where changes in the sign of the electric field wave amplitude corresponds to changes in the electric field direction.

However, there is some correspondence between increasing electric field wave amplitudes in regions of the crustal magnetic field cusps and the angle of LPW measurements deviating slightly from angles perpendicular to the magnetic field. This might serve as some indication for the strong parallel components in the electric field wave amplitude not covered by LPW in regions of the crustal magnetic field cusps. The presence of small scale fluctuations in the parallel electric field is supported by the brief observations during electron spikes D and E of additional energetic peaks in electron energy flux (cf. Figures 3e–3h). Due to the small gyroscales of electrons the small scale variations in the field aligned electric field potential may act as a DC accelerating field of electrons over small scales. However, such small scale electric fields will be in competition with plasma drifts that move electrons in and out of the small scale potential structures. This may explain why electron energy spectra are measured with a mixture of peaks of accelerated electrons in addition to unaccelerated but heated electron spectra.

Also, the periods of increased electric field wave amplitude fluctuations during ion spikes 1 and 6 coincide with ion velocity distributions showing the possible conservation of the first adiabatic invariant by H^+ ions in a magnetic field mirror field. Perpendicular electric fields may produce perpendicular energization of ions through transverse wave heating (André & Yau, 1997), acceleration of nonadiabatic ions (Cole, 1976) or a combination of both (Lindstedt et al., 2010). This may relate to characteristics of Figures 7b and 7d showing parallel ions directed toward Mars extending asymmetrically to larger pitch angles for increasing parallel velocity and ions traveling at away from Mars at conical pitch angles (André & Yau, 1997; Øieroset et al., 1999).

6. Spatial Ion Energy Dispersions of Kilo-Electron-Volt Ions

Figure 9 shows energy-time spectrograms using a linear energy scale shown on the left-hand axis to highlight the appearance of energy dispersed structures from kilo-electron-volt ions observed between the appearance of ion spikes 2 and 5 and respective kilo-electron-volt ion bands observed close to each ion spike. This is compared to the altitude of MAVEN as shown by the dashed line and right-hand axis. The ion energy dispersions show hallmarks of a presence of electric fields. First is the linear dependence of ion energy (E/q) with time and altitude and second the tone of the energy dispersion is arranged with the spacecraft motion with respect to Mars. Such features have been reported in cases of energy dispersed structures showing the extraction of ions from the Martian magnetosphere by large electric fields (Dubinin, Lundin, et al., 2006). However, the energy dispersed structures reported here are for ions precipitating toward Mars and would therefore be related to the deceleration of ions rather than the acceleration of ions described by Dubinin, Lundin, et al. (2006). The form of the energy dispersed ions reported here at energies >1.4 keV also follow features of modeled solar wind proton energy spectrum showing the deceleration by large electric fields of solar wind protons directed toward magnetic anomalies on the Lunar surface (Giacalone & Hood, 2015; Poppe et al., 2016).

In the case of energy dispersion of ions $E > 1.4$ keV on 26 October 2015, there is a change in 4.75-keV ion energy over 62 km in altitude and approximately 372 km along the MAVEN flight path (93 s at 4 km/s). This would relate to electric fields as large as ~ 80 mV/m in the radial extent and ~ 10 mV/m along the orbit path of MAVEN. In the case of energy dispersion of ions $E > 1.4$ keV on 2 June 2015, there is a change in 9-keV ion energy over 3.2 km in altitude and approximately 240 km along the MAVEN flight path (60 s at 4 km/s). This would relate to electric fields as large as ~ 3 V/m in the radial extent and ~ 40 mV/m along the orbit path of MAVEN. It does not seem conceivable electric fields this large can be present over the scale size of the observed

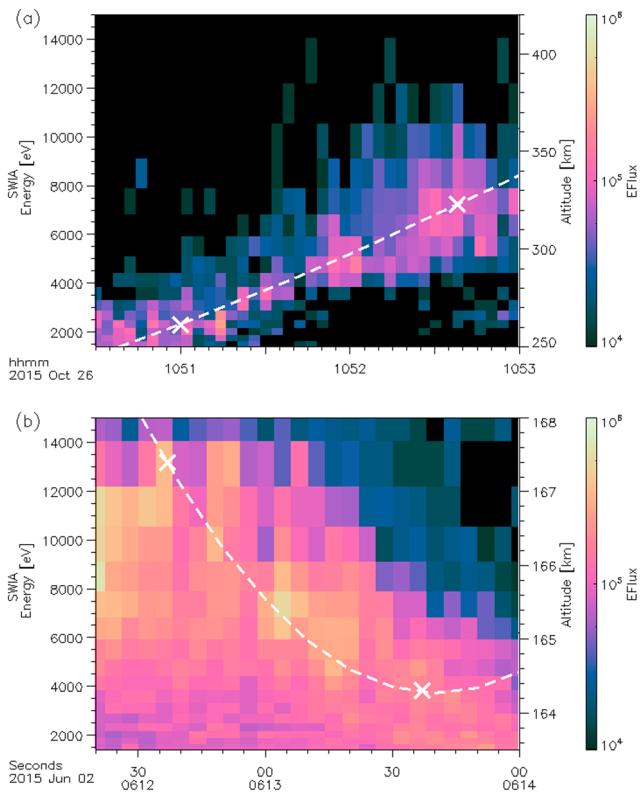


Figure 9. Examples of energy dispersed kilo-electron-volt ions that mark the transition between kilo-electron-volt ion bands features and the appearance of (a) broad energy range ion spike 2 observed on 26 October 2015 and (b) broad energy range ion spike 5 observed on 2 June 2015. Dashed lines demonstrate the linear dependence of ion energy with altitude and cross marks show the limits used for determining an electric field strength associated with the deceleration of the ions.

ion energy dispersions without the occurrence of other noticeable effects. For example, the bulk acceleration of the local thermal ion population away from Mars or an equivalent acceleration of electrons toward Mars might be expected but are not observed.

Instead, the energy dispersed structures presented here for ions $E > 1.4$ keV could be interpreted as the velocity selection effect illustrated in Figure 8b, due to a combination of the orientation of the magnetic field and trajectories of pickup ions with different energies. In this interpretation O^+ pickup ions that have spent more time being accelerated in the pickup process have higher energy and are on more anti-Sunward trajectories and will experience magnetic reflection when encountering regions of stronger radial crustal magnetic field. This could then account for the cutoff in time of higher energy ions (e.g., $E > 4$ keV) in the kilo-electron-volt ion-band feature. Whereas O^+ pickup ions that have spent less time being accelerated have lower energy and are on trajectories that are more directed toward Mars. These ions will be preferentially selected in radial crustal magnetic field regions due to their field aligned pitch angles resulting a beam of kilo-electron-volt ions precipitating toward Mars. The tone of energy dispersion could relate to the direction of MAVEN with respect to Mars and altitude since energetic anti-Sunward ions will experience greater magnetic reflection from the increased crustal magnetic field strengths at lower altitudes.

7. Energy Deposition From Precipitating Ions in Radial Crustal Magnetic Fields

Occurring at low altitudes, below 300 km, the kilo-electron-volt ion precipitation observed during ion spikes studied here on the dayside of Mars may present important periods of energy deposition, although episodic and localized. In comparison to solar EUV energy absorbed below 300 km on the dayside by the Martian atmosphere, contributions from electron precipitation and energy from electromagnetic waves are negligible. Energy from electromagnetic waves may play an important role in the outflow of

ions in regions of collisionless plasma at higher altitudes (Ergun et al., 2006), whereas electron precipitation is the dominant source of energy input into the nightside Martian atmosphere (Lillis & Fang, 2015; Fillingim et al., 2010). Modeling by Fang et al. (2013) shows that pickup O^+ ions precipitating toward Mars from the -E hemisphere of the Mars-Sun-Electric field (MSE) frame can result in significant energy deposition on the dayside of Mars compared to input from solar EUV energy, varying between negligible to very important effects on the thermosphere when upstream solar wind conditions vary from normal to extreme.

In the case of the ion precipitation from ion spike 2 presented in Figure 5, the energy deposition between 1.3 and 7.5 keV from the accelerated beam of O^+ ions in energy flux is calculated by integrating SWIA energy flux measurements over the energy and solid angle corresponding to the observation of the ion beam and results in $5.5 \times 10^{-7} \text{ W/m}^2$ ($3.5 \times 10^8 \text{ eV}/(\text{cm}^2 \cdot \text{s})$). The mass deposition in number flux is calculated by integrating SWIA flux measurements over the energy and solid angle corresponding to the observation of the ion beam and results in $1.4 \times 10^5 \text{ #}/(\text{cm}^2 \cdot \text{s})$. In the case of the ion precipitation presented in Figure 6, the energy deposition between 1.3 and 9.0 keV from the accelerated ion beam, assumed as O^+ ions, in energy flux is $3.6 \times 10^{-6} \text{ W/m}^2$ ($2.3 \times 10^9 \text{ eV}/(\text{cm}^2 \cdot \text{s})$) and mass deposition in number flux is $7.1 \times 10^5 \text{ #}/(\text{cm}^2 \cdot \text{s})$. This compares to the average SWIA ion precipitating flux for radial magnetic field orientations from the study by Hara et al. (2018), resulting in an energy deposition between 1.3 and 9.0 keV for energy flux over a 70° precipitating cone angle, $2.9 \times 10^{-6} \text{ W/m}^2$ ($1.8 \times 10^9 \text{ eV}/(\text{cm}^2 \cdot \text{s})$) and mass deposition in number flux, $5.3 \times 10^5 \text{ #}/(\text{cm}^2 \cdot \text{s})$.

The most significant effect from ion precipitation on the dayside of Mars may be from momentum transfer during ion-neutral collisions where a sputtering process can result in the escape of atmosphere (Johnson et al., 2000; Leblanc & Johnson, 2001; Luhmann & Kozyra, 1991). Relationships derived by Wang et al. (2015) from the modeling of O^+ sputtering effects can be applied to MAVEN observations to estimate possible escape rates.

Using the values for precipitating energy flux and number flux determined from Figure 5 in equation 14 from Wang et al. (2015) results in an escape rate of 6.0×10^4 /(cm².s) for precipitation of the accelerated ion beam from 1.4 to 7.5 keV and 9.0×10^4 /(cm².s) for the broader precipitation of ions between 25 and 0.1 keV. Using the sputtering yield tables for O given by Figure A1 from Wang et al. (2015), a maximum yield of $\sim 450\%$ for precipitating 1.4 to 7.5 keV O⁺ ions with incident angles of 0° - 20° results in an escape of 6.3×10^5 /(cm².s), and a maximum sputtering yield of $\sim 100\%$ for precipitating 25 eV to 0.1 keV O⁺ ions with incident angles of 0° - 45° results in an escape of 1.5×10^6 /(cm².s).

8. Summary and Conclusions

For the first time at Mars, simultaneous ion, electron, magnetic field vector, and electric field wave measurements from the MAVEN PFP instrument suite have been used to study the plasma transport processes and associated electrodynamic effects related to broad energy range ion spikes of ion energy flux in regions of the low-altitude (>300 km) radial crustal magnetic field, aka cusps, on the dayside of Mars. This also allows the unambiguous characterization for the kinetic behavior of ions from ion velocity distributions formed with use of in situ vector measurements of the magnetic field, which has not been achieved before at Mars from measurements in the low-altitude crustal magnetic fields. Time periods have been chosen that show the extraordinary coincidence of signatures of energy flux ion spikes observed in radial crustal magnetic fields and energy-time bands of kilo-electron-volt ions that extend over horizontal crustal magnetic fields.

The ion spikes are characterized by the precipitation toward Mars of different ion populations; planetary-like O⁺ and O₂⁺ ions and magnetosheath-like H⁺ ions and when coinciding with kilo-electron-volt ion energy-time bands also involved kilo-electron-volt O⁺ ions typical of ions picked-up by the solar wind. The ion spikes presented here are also observed alongside the precipitation of energetic electrons or electron spikes in energy flux along radial magnetic field lines that have been assumed as being closed.

Populations of H⁺ ion $E < 1.4$ keV and O⁺ and O₂⁺ ions $E < 0.1$ keV are observed with broad ion velocity distributions precipitating toward Mars and are interpreted as ions flowing from higher altitude crustal magnetic fields. This may occur as a result of the injection of ions following either magnetic reconnection or a filling of the loss cone by the pitch angle scattering from nonadiabatic effects or wave particle interactions.

Depending on ion energy (H⁺ $E > 320$ eV) or mass (O⁺ and O₂⁺ $E < 0.1$ keV), ion velocity distributions measured during the spikes show ions precipitating from above can have nonadiabatic characteristics possibly retained after being transported from regions of weaker magnetic field. Also, at the same time a reflected component of ions and a loss cone is observed for ions moving away from Mars and this is indicative of the conservation of first adiabatic invariant in a mirror field for ions transported from lower altitudes. This is further exemplified by observations around ~ 175 km altitude of nongyrotropic partial ring distributions of H⁺ ions precipitating toward Mars. Distributions of mirroring ions may be unstable to plasma waves and perpendicular ion heating. This is supported by the first tentative observations of ion conics directed away from Mars in radial crustal magnetic fields. Considering only the effects of a charge exchange process on a mirroring population of precipitating H⁺ ions, could result in an additional hydrogen escape from Mars if the original source of the precipitating H⁺ ions is from the hot ion corona of Mars instead of the solar wind. Evidence of the adiabatic behavior of ions is observed in spite of the parameter of adiabaticity from the expected radius of curvature of the crustal magnetic field not supporting adiabatic effects. This would suggest ions are injected with highly field aligned distributions at higher altitudes or that the crustal magnetic fields have a radius of curvature that is much larger than expected.

The precipitating ion and electron spikes also occur alongside remarkably large perturbations in the background magnetic field, with magnitudes of up to 60 nT and large wave amplitudes in the electric field. These large electric field wave amplitudes are measured at perpendicular to oblique angles to the local magnetic field and occur over short time scales, typically between 1 and 10 mV/m and with large outliers between 20 and 38 mV/m. Greater fluctuations in the electric field in regions of the crustal magnetic field cusps are associated with LPW measurements deviating slightly from angles perpendicular to the magnetic field, as well as ion velocity distributions that showed a combination of nongyrotropic partial ring distributions of H⁺ ions with features suggestive of a transverse heating/energization of ions precipitating toward Mars and ions moving away from Mars at conical angles to the magnetic field.

The measurement of fluctuating electric fields with perpendicular to oblique angles to the magnetic field could translate to small scale double layer structures and a series of small scale field aligned electric fields or potential drops. Indeed, brief observations of field aligned peaked electrons up to energies of 150 eV precipitating toward Mars would support the possibility of a small-scale DC accelerating fields. It is proposed that the presence of large electric fields measured in the radial crustal magnetic field regions could be supported by a charge separation dynamo as caused by the different altitudes observed for reflected electrons and ions and mirroring of H⁺ ions around ~175 km.

The precipitating ions >1.4 keV, as associated with O⁺ ions, occur as accelerated ion beams as would occur due to the injection of ions accelerated externally, but are also observed as field aligned ions that have been heated by a more local process. Although, it is not known if the heating is caused by the energization or deceleration of ions. Energy dispersed structures of O⁺ ions that could signify the deceleration of ions by electric fields as large as ~3 V/m in the radial extent and ~40 mV/m along the MAVEN orbit path are instead interpreted as a velocity selection effect of pickup ions over radial crustal magnetic field. That is ions picked up at closer distances to Mars that are of lower energy have more Marsward (field aligned) trajectories and are preferentially selected in regions of radial crustal magnetic fields. This compares to ions picked-up at further distances that are of higher energy, which have more anti-Sunward trajectories and will experience greater reflection in regions of radial crustal magnetic fields and also as the strength of the magnetic field increases in such regions.

The precipitating O⁺ ions observed during the ion spikes reported here will have implications for sputtering and localized atmospheric heating, with the calculation of energy deposition rates as large as 3.6×10^{-6} W/m² and mass deposition rates as large as 7.1×10^5 #/(cm².s). The total sputtering escape rates of 1.5×10^5 /(cm².s) and 2.1×10^6 /(cm².s) are calculated using the sputtering response relation and O sputtering yield tables from Wang et al. (2015), respectively. Considering ion spike 2 is observed over an expanse of 0.7° latitude at an altitude of around 260 km, that is, a flux tube of around 22-km radius with a cross-sectional area of roughly 1.5×10^3 km², this could relate to a total mass loss of O atoms of ~ 6×10^{-8} kg/s (~ 5×10^{-3} kg/day), as derived from sputtering response relations and ~ 8×10^{-7} kg/s (~ 70×10^{-3} kg/day), as derived from sputtering yield tables from Wang et al. (2015).

Acknowledgments

The MAVEN mission is supported by NASA through the Mars Scout program. All data presented as part of this paper are available on the Planetary Data System (<https://pds-ppi.igpp.ucla.edu/search/?sc=MAVEN>).

References

- Acuña, M. H., Connerney, J. E. P., Wasilewski, P., Lin, R. P., Anderson, K. A., Carlson, C. W., et al. (1998). Magnetic field and plasma observations at Mars: Initial results of the Mars Global Surveyor mission. *Science*, *279*, 1676–1680. <https://doi.org/10.1126/science.279.5357.1676>
- Alem, F., & Delcourt, D. C. (1995). Nonadiabatic precipitation of ions at the cusp equatorward edge. *Journal of Geophysical Research*, *100*(A10), 19321–19328. <https://doi.org/10.1029/95JA01160>
- Andersson, L., Ergun, R. E., Delory, G. T., Eriksson, A., Westfall, J., Reed, H. et al. (2015). The Langmuir Probe and Waves (LPW) Instrument for MAVEN. *Space Science Reviews*, *195*, 173–198. <https://doi.org/10.1007/s11214-015-0194-3>
- André, M., & Yau, A. (1997). Theories and observations of ion energization and outflow in the high latitude magnetosphere. *Space Science Reviews*, *80*, 27–48. <https://doi.org/10.1023/A:1004921619885>
- Bertaux, J.-L., Leblanc, F., Witasse, O., Quemerais, E., Liliensten, J., Stern, S. A., et al. (2005). Discovery of an aurora on Mars. *Nature*, *435*, 790–794. <https://doi.org/10.1038/nature03603>
- Block, L. P. (1988). Acceleration of auroral particles by magnetic-field aligned electric fields. *Astrophysics and Space Science*, *144*, 135–147. <https://doi.org/10.1007/BF00793177>
- Bouhram, M., Dubouloz, N., Malingre, M., Jasperse, J. R., Pottelette, R., Senior, C., et al. (2002). Ion outflow and associated perpendicular heating in the cusp observed by Interball Auroral Probe and Fast Auroral Snapshot. *Journal of Geophysical Research*, *107*(A2), 102310–1029. <https://doi.org/10.1029/2001JA000091>
- Brain, D. A., Halekas, J. S., Lillis, R. J., Mitchell, D. L., Lin, R. P., & Crider, D. H. (2005). Variability of the altitude of the Martian sheath. *Geophysical Research Letters*, *32*, L18203. <https://doi.org/10.1029/2005GL023126>
- Brain, D. A., Halekas, J. S., Peticolas, L. M., Lin, R. P., Luhmann, J. G., Mitchell, D. L., et al. (2006). On the origin of aurorae on Mars. *Geophysical Research Letters*, *33*, L01201. <https://doi.org/10.1029/2005GL024782>
- Brain, D. A., Halekas, J. S., Peticolas, L. M., Lin, R. P., Luhmann, J. G., Mitchell, D. L., et al. (2010). On the origin of aurorae on Mars. *Geophysical Research Letters*, *33*, L01201. <https://doi.org/10.1029/2005GL024782>
- Brain, D. A., Lillis, R. J., Mitchell, D. L., Halekas, J. S., & Lin, R. P. (2007). Electron pitch angle distributions as indicators of magnetic field topology near Mars. *Journal of Geophysical Research*, *112*, A09201. <https://doi.org/10.1029/2007JA012435>
- Brecht, S. H., & Ledvina, S. A. (2012). Control of ion loss from Mars during solar minimum. *Earth, Planets and Space*, *64*, 165–178. <https://doi.org/10.5047/eps.2011.05.037>
- Briggs, J. A., Brain, D. A., Cartwright, M. L., Eastwood, J. P., & Halekas, J. S. (2012). A statistical study of flux ropes in the martian magnetosphere. *Planet Space Science*, *59*, 1498–1505. <https://doi.org/10.1016/j.pss.2011.06.010>
- Buchner, J., & Zelenyi, L. M. (1986). Deterministic chaos in the dynamics of charged particles near a magnetic field reversal. *Physics Letters A*, *118*, 395. [https://doi.org/10.1016/0375-9601\(86\)90268-9](https://doi.org/10.1016/0375-9601(86)90268-9)
- Buchner, J., & Zelenyi, L. M. (1989). Regular and chaotic charged particle motion in magnetotail-like field reversals: 1. Basic theory of trapped motion. *Journal of Geophysical Research*, *94*(11), 821. <https://doi.org/10.1029/JA094iA09p11821>

- Cattell, C., & Hudson, M. (1982). Flute mode waves near the lower hybrid frequency excited by ion rings in velocity space. *Geophysical Research Letters*, 9, 1167–1170. <https://doi.org/10.1029/GL0091010p01167>
- Cole, K. D. (1976). Effects of crossed magnetic and (spatially dependent) electric fields on charged particle motion. *Planetary and Space Science*, 24, 515–518. [https://doi.org/10.1016/0032-0633\(76\)90096-9](https://doi.org/10.1016/0032-0633(76)90096-9)
- Collinson, G., David, M., Glocer, A., Grebowsky, J., Peterson, W. K., Connerney, J., et al. (2015). Electric Mars: The first direct measurement of an upper limit for the Martian “polar wind” electric potential. *Geophysical Research Letters*, 42, 9128–9134. <https://doi.org/10.1002/2015GL065084>
- Connerney, J. E. P., Acuña, M. H., Ness, N. F., Kletetschka, G., Mitchell, D., Lin, R. P., & Reme, H. (2005). Tectonic implications of Mars crustal magnetism. *Proceedings of the National Academy of Sciences*, 102(42), 14970–14975. <https://doi.org/10.1073/pnas.0507469102>
- Connerney, J. E. P., Acuña, M. H., Wasilewski, P. J., Kletetschka, G., Ness, N. F., Rème, H., et al. (2001). The global magnetic field of Mars and implications for crustal evolution. *Geophysical Research Letters*, 28, 4015–4018. <https://doi.org/10.1029/2001GL013619>
- Connerney, J. E. P., Espley, J. R., DiBraccio, G. A., Gruesbeck, J. R., Oliverson, R. J., Mitchell, D. L., et al. (2015). First results of the MAVEN magnetic field investigation. *Geophysical Research Letters*, 42, 8819–8827. <https://doi.org/10.1002/2015GL065366>
- Connerney, J. E. P., Espley, J. R., Lawton, P., Murphy, S., Odom, J., Oliverson, R., & Sheppard, D. (2015). The MAVEN Magnetic Field Investigation. *Space Science Reviews*, 195, 257–291. <https://doi.org/10.1007/s11214-015-0169-4>
- Curry, S. M., Luhmann, J., Yingjuan, M. J., Michael, L., Dong, C., & Hara, T. (2015). Comparative pick-up ion distributions at Mars and Venus: Consequences for atmospheric deposition and escape. *Planetary and Space Science*, 115, 35–47. <https://doi.org/10.1016/j.pss.2015.03.026>
- Deca, J., Divin, A., Lembège, B., Horányi, M., Markidis, S., & Lapenta, G. (2015). General mechanism and dynamics of the solar wind interaction with lunar magnetic anomalies from 3-D particle-in-cell simulations. *Journal of Geophysical Research: Space Physics*, 120, 6443–6463. <https://doi.org/10.1002/2015JA021070>
- Dong, C., Bougher, S. W., Ma, Y., Toth, G., Lee, Y., Nagy, A. F., et al. (2015). Solar wind interaction with the Martian upper atmosphere: Crustal field orientation, solar cycle, and seasonal variations. *Journal of Geophysical Research: Space Physics*, 120, 7857–7872. <https://doi.org/10.1002/2015JA020990>
- Dubinin, E., Chanteur, G., Fraenz, M., & Woch, J. (2008). Field-aligned currents and parallel electric field potential drops at Mars. Scaling from the Earth? aurora. *Planetary and Space Science*, 56, 868–872. <https://doi.org/10.1016/j.pss.2007.01.019>
- Dubinin, E., Fraenz, M., Fedorov, A., Lundin, R., Edberg, N., Duru, F., & Vaisberg, O. (2011). Ion energization and escape on Mars and Venus. *Space Science Review*, 162, 173–211. <https://doi.org/10.1007/s11214-011-9831-7>
- Dubinin, E., Fraenz, M., Woch, J., Barabash, S., & Lundin, R. (2009). Long-lived auroral structures and atmospheric losses through auroral flux tubes on Mars. *Geophysical Research Letters*, 36, L08108. <https://doi.org/10.1029/2009GL038209>
- Dubinin, E., Fraenz, M., Woch, J., Barabash, S., Lundin, R., & Yamauchi, M. (2006). Hydrogen exosphere at Mars: Pickup protons and their acceleration at the bow shock. *Geophysical Research Letters*, 33, L22103. <https://doi.org/10.1029/2006GL027799>
- Dubinin, E., Lundin, R., Fränz, M., Woch, J., Barabash, S., Fedorov, A., et al. (2006). Electric fields within the martian magnetosphere and ion extraction: ASPERA-3 observations. *Icarus*, 182, 337–342. <https://doi.org/10.1016/j.icarus.2005.05.022>
- Dubinin, E., Lundin, R., Norberg, O., & Pissarenko, N. (1993). Ion acceleration in the Martian tail: Phobos observations. *Journal of Geophysical Research*, 98, 3991–3997. <https://doi.org/10.1029/92JA02233>
- Dubinin, E., Lundin, R., & Schwingenschuh, K. (1994). Solar wind electrons as tracers of the Martian magnetotail topology. *Journal of Geophysical Research*, 99(A11), 21,233–21,240. <https://doi.org/10.1029/94JA01271>
- Ergun, R. E., Andersson, L., Peterson, W. K., Brain, D., Delory, G. T., Mitchell, D. L., et al. (2006). Role of plasma waves in Mars’ atmospheric loss. *Geophysical Research Letters*, 33, L14103. <https://doi.org/10.1029/2006GL025785>
- Fang, X., Bougher, S. W., Johnson, R. E., Luhmann, J. G., Ma, Y., Wang, Y.-C., & Liemohn, M. W. (2013). The importance of pickup oxygen ion precipitation to the Mars upper atmosphere under extreme solar wind conditions. *Geophysical Research Letters*, 40, 1922–1927. <https://doi.org/10.1002/grl.50415>
- Fang, X., Liemohn, M. W., Nagy, A. F., Luhmann, J. G., & Ma, Y. (2010). On the effect of the Martian crustal magnetic field on atmospheric erosion. *Icarus*, 206, 130–138. <https://doi.org/10.1016/j.icarus.2009.01.012>
- Fang, X., Ma, Y., Brain, D., Dong, Y., & Lillis, R. (2015). Control of Mars global atmospheric loss by the continuous rotation of the crustal magnetic field: A time-dependent MHD study. *Journal of Geophysical Research: Space Physics*, 120, 10,926–10,944. <https://doi.org/10.1002/2015JA021070>
- Fillingim, M. O., Peticolas, L. M., Lillis, R. J., Brain, D. A., Halekas, J. S., Lummerzheim, D., & Bougher, S. W. (2010). Localized ionization patches in the nighttime ionosphere of Mars and their electrodynamic consequences. *Icarus*, 206, 112–119. <https://doi.org/10.1016/j.icarus.2009.03.005>
- Fowler, C. M., Andersson, L., Halekas, J., Espley, J. R., Mazelle, C., Coughlin, E. R., et al. (2017). Electric and magnetic variations in the near-Mars environment. *Journal of Geophysical Research: Space Physics*, 122, 8536–8559. <https://doi.org/10.1002/2016JA023411>
- Frahm, R. A., Winningham, J. D., Sharber, J. R., Scherrer, J. R., Jeffers, S. J., Coates, A. J., et al. (2006). Carbon dioxide photoelectron energy peaks at Mars. *Icarus*, 182, 371–382. <https://doi.org/10.1016/j.icarus.2006.01.014>
- Fränz, M., Dubinin, E., Nielsen, E., Woch, J., Barabash, S., Lundin, R., & Fedorov, A. (2010). Transterminator ion flow in the Martian ionosphere. *Planetary and Space Science*, 58, 1442–1454. <https://doi.org/10.1016/j.pss.2010.06.009>
- Fränz, M., Winningham, J. D., Dubinin, E., Roussos, E., Woch, J., Barabash, S., et al. (2006). Plasma intrusion above Mars crustal fields—Mars Express ASPERA-3 observations. *Icarus*, 182, 406–412. <https://doi.org/10.1016/j.icarus.2005.11.016>
- Futaana, Y., Barabash, S., Wieser, M., Lue, C., Wurz, P., Vorburger, A., et al. (2013). Remote energetic neutral atom imaging of electric potential over a lunar magnetic anomaly. *Geophysical Research Letters*, 40, 262–266. <https://doi.org/10.1002/grl.50135>
- Gérard, J.-C., Soret, L., Libert, L., Lundin, R., Stiepen, A., Radioti, A., & Bertaux, J.-L. (2015). Concurrent observations of ultraviolet aurora and energetic electron precipitation with Mars Express. *Journal of Geophysical Research: Space Physics*, 120, 6749–6765. <https://doi.org/10.1002/2015JA021150>
- Giacalone, J., & Hood, L. L. (2015). Hybrid simulation of the interaction of solar wind protons with a concentrated lunar magnetic anomaly. *Journal of Geophysical Research: Space Physics*, 120, 4081–4094. <https://doi.org/10.1002/2014JA020938>
- Gorney, D. J. (1983). An alternative interpretation of ion ring distributions observed by the S3-3 satellite. *Geophysical Research Letters*, 10, 417–420. <https://doi.org/10.1029/GL010i005p00417>
- Grigorenko, E. E., Hoshino, M., Hirai, M., Mukai, T., & Zelenyi, L. M. (2009). “Geography” of ion acceleration in the magnetotail: X-line versus current sheet effects. *Journal of Geophysical Research*, 114, A03203. <https://doi.org/10.1029/2008JA013811>
- Halekas, J. S., Brain, D. A., Lin, R. P., Luhmann, J. G., & Mitchell, D. L. (2008). Distribution and variability of accelerated electrons at Mars. *Advances in Space Research*, 195, 125–151. <https://doi.org/10.1016/j.asr.2007.01>

- Halekas, J. S., Lillis, R. J., Mitchell, D. L., Cravens, T. E., Mazelle, C., Connerney, J. E. P., et al. (2015). MAVEN observations of solar wind hydrogen deposition in the atmosphere of Mars. *Geophysical Research Letters*, *42*, 8901–8909. <https://doi.org/10.1002/2015GL064693>
- Halekas, J. S., Taylor, E. R., Dalton, G., Johnson, G., Curtis, D. W., McFadden, J. P., et al. (2015). The Solar Wind Ion Analyzer for MAVEN. *Space Science Reviews*, *95*, 125–151. <https://doi.org/10.1007/s11214-013-0029-z>
- Hara, T., Brain, D. A., Mitchell, D. L., Luhmann, J. G., Seki, K., Hasegawa, H., et al. (2017). MAVEN observations of a giant ionospheric flux rope near Mars resulting from interaction between the crustal and interplanetary draped magnetic fields. *Journal of Geophysical Research: Space Physics*, *122*, 828–842. <https://doi.org/10.1002/2016JA023347>
- Hara, T., Luhmann, J. G., Leblanc, F., Curry, S. M., Halekas, J. S., Seki, K., et al. (2018). Evidence for crustal magnetic field control of ions precipitating into the upper atmosphere of Mars. *Journal of Geophysical Research: Space Physics*, *122*, 8572–8586. <https://doi.org/10.1029/2017JA024798>
- Hara, T., Luhmann, J. G., Leblanc, F., Curry, S. M., Seki, K., Brain, D. A., et al. (2017). MAVEN observations on a hemispheric asymmetry of precipitating ions toward the Martian upper atmosphere according to the upstream solar wind electric field. *Journal of Geophysical Research: Space Physics*, *122*, 1083–1101. <https://doi.org/10.1002/2016JA023348>
- Harada, Y., Halekas, J. S., McFadden, J. P., Mitchell, D. L., Mazelle, C., Connerney, J. E. P., et al. (2015). Magnetic reconnection in the near-Mars magnetotail: MAVEN observations. *Geophysical Research Letters*, *42*, 8838–8845. <https://doi.org/10.1002/2015GL065004>
- Harada, Y., Mitchell, D. L., Halekas, J. S., McFadden, J. P., Mazelle, C., Connerney, J. E. P., et al. (2016). MAVEN observations of energy-time dispersed electron signatures in Martian crustal magnetic fields. *Geophysical Research Letters*, *43*, 939–944. <https://doi.org/10.1002/2015GL067040>
- Hudson, M. K., & Roth, I. (1986). Ion heating in the cusp. In T. Chang et al. (Eds.), *Ion Acceleration in the Magnetosphere and Ionosphere* (Vol. 38, pp. 271–281). Washington, DC: American Geophysical Union. <https://doi.org/10.1029/GM038p0271>
- Jakosky, B. M., Lin, R. P., Grebowsky, J. M., Luhmann, J. G., Mitchell, D. F., Beutelschies, G., et al. (2015). The Mars Atmosphere and Volatile Evolution (MAVEN) Mission. *Space Science Reviews*, *195*, 3–48. <https://doi.org/10.1007/s11214-015-0139-x>
- Johnson, R. E., Schnellenberger, D., & Wong, M. C. (2000). The sputtering of an oxygen thermosphere by energetic O⁺. *Journal of Geophysical Research*, *105*(E1), 1659–1670. <https://doi.org/10.1029/1999JE001058>
- Kallio, E., Fedorov, A., Budnik, E., Barabash, S., Jarvinen, R., & Janhunen, P. (2008). On the properties of O⁺ and O₂⁺ ions in a hybrid model and in Mars Express IMA/ASPERA-3 data: A case study. *Planetary and Space Science*, *56*, 1204–1213. <https://doi.org/10.1016/j.pss.2008.03.007>
- Kallio, E., Jarvinen, R., Dyadechkin, S., Wurz, P., Barabash, S., Alvarez, F., et al. (2012). Kinetic simulations of finite gyroradius effects in the lunar plasma environment on global, meso, and microscales. *Planetary and Space Science*, *74*, 146–155. <https://doi.org/10.1016/j.pss.2012.09.012>
- Knudsen, W., Spenner, K., & Miller, K. (1981). Anti-solar acceleration of ionospheric plasma across the Venus terminator. *Geophysical Research Letters*, *8*, 241–244. <https://doi.org/10.1029/GL008i003p00241>
- Leblanc, F., & Johnson, R. E. (2001). Sputtering of the Martian atmosphere by solar wind pick-up ions. *Planetary and Space Science*, *49*, 645–656. <https://doi.org/10.1016/j.pss.2015.03.026>
- Leblanc, F., & Johnson, R. E. (2002). Role of molecular species in pickup ion sputtering of the Martian atmosphere. *Journal of Geophysical Research*, *107*(E2), 5010. <https://doi.org/10.1029/2000JE001473>
- Li, L., Zhang, Y., Feng, Y., Fang, X., & Ma, Y. (2011). Oxygen ion precipitation in the Martian atmosphere and its relation with the crustal magnetic fields. *Journal of Geophysical Research*, *116*, A08204. <https://doi.org/10.1029/2010JA016249>
- Lillis, R. J., & Fang, X. (2015). Electron impact ionization in the Martian atmosphere: Interplay between scattering and crustal magnetic field effects. *Journal of Geophysical Research: Planets*, *120*, 1332–1345. <https://doi.org/10.1002/2015JE004841>
- Lillis, R. J., Halekas, J. S., Fillingim, M. O., Poppe, A. R., Collinson, G., Brain, D. A., & Mitchell, D. L. (2018). Field-aligned electrostatic potentials above the Martian exobase from MGS electron reflectometry: Structure and variability. *Journal of Geophysical Research: Planets*, *123*, 67–92. <https://doi.org/10.1002/2017JE005395>
- Lindstedt, T., Khotyaintsev, Y. V., Vaivads, A., André, M., Nilsson, H., & Waara, M. (2010). Oxygen energization by localized perpendicular electric fields at the cusp boundary. *Geophysical Research Letters*, *37*, L09103. <https://doi.org/10.1029/2010GL043117>
- Luhmann, J. G., & Kozyra, J. U. (1991). Dayside pickup oxygen ion precipitation at Venus and Mars: Spatial distributions, energy deposition and consequences. *Journal of Geophysical Research*, *96*(A4), 5457–5467. <https://doi.org/10.1029/90JA01753>
- Lundin, R., Barabash, S., Yamauchi, M., Nilsson, H., & Brain, D. (2011). On the relation between plasma escape and the Martian crustal magnetic field. *Geophysical Research Letters*, *38*, L02102. <https://doi.org/10.1029/2010GL046019>
- Lundin, R., Winningham, D., Barabash, S., Frahm, R., Brain, D., Nilsson, H., et al. (2006). Auroral plasma acceleration above Martian magnetic anomalies. *Space Science Reviews*, *126*, 333–354. <https://doi.org/10.1007/s11214-006-9086-x>
- Lundin, R., Winningham, D., Barabash, S., Frahm, R., Holmström, M., Sauvaud, J.-A., et al. (2006). Plasma acceleration above Martian magnetic anomalies. *Science*, *311*, 980. <https://doi.org/10.1126/science.1122071>
- Ma, Y., Fang, X., Russell, C. T., Nagy, A. F., Toth, G., Luhmann, J. G., et al. (2014). Effects of crustal field rotation on the solar wind plasma interaction with Mars. *Geophysical Research Letters*, *41*, 6563–6569. <https://doi.org/10.1002/2014GL060785>
- Mahaffy, P. R., Benna, M., Elrod, M., Yelle, R. V., Bougher, S. W., Stone, S. W., & Jakosky, B. M. (2015). Structure and composition of the neutral upper atmosphere of Mars from the MAVEN NGIMS investigation. *Geophysical Research Letters*, *42*, 8951–8957. <https://doi.org/10.1002/2015GL065329>
- Mahaffy, P. R., Benna, M., King, T., Harpold, D., Arvey, R., Barciniak, M., et al. (2015). The neutral gas and ion mass spectrometer on the Mars Atmosphere and Volatile Evolution Mission. *Space Science Reviews*, *195*, 49–73. <https://doi.org/10.1007/s11214-014-0091-1>
- Martin, R. F., Delcourt, D., Holland, D. L., & Asbury, M. J. (2000). Magnetotail particle distributions associated with pitch angle isotropization. *Journal of Atmospheric and Solar-Terrestrial Physics*, *62*, 513–519. [https://doi.org/10.1016/S1364-6826\(00\)00020-1](https://doi.org/10.1016/S1364-6826(00)00020-1)
- McFadden, J. P., Kortmann, O., Curtis, D., Dalton, G., Johnson, G., Abiad, R., et al. (2015). MAVEN SupraThermal and Thermal Ion Composition (STATIC) Instrument. *Space Science Reviews*, *195*, 199–256. <https://doi.org/10.1007/s11214-015-0175-6>
- Mitchell, D. L., Lin, R. P., Mazelle, C., Rème, H., Cloutier, P. A., Connerney, J. E. P., et al. (2001). Probing Mars' crustal magnetic field and ionosphere with the MGS Electron Reflectometer. *Journal of Geophysical Research*, *106*(E10), 23,419–23,427. <https://doi.org/10.1029/2000JE001435>
- Mitchell, D. L., Mazelle, C., Sauvaud, J.-A., Thocaven, J.-J., Rouzaud, J., Fedorov, A., et al. (2016). The MAVEN Solar Wind Electron Analyzer. *Space Science Review*, *200*, 495–528. <https://doi.org/10.1007/s11214-015-0232-1>
- Morschhauser, A., Lesur, V., & Grott, M. (2014). A spherical harmonic model of the lithospheric magnetic field of Mars. *Journal of Geophysical Research: Planets*, *119*, 1162–1188. <https://doi.org/10.1002/2013JE004555>
- Nagy, A. F., Winterhalter, D., Sauer, K., Cravens, T. E., Brecht, S., Mazelle, C., et al. (2004). The plasma environment of Mars. *Space Science Review*, *111*, 33–114. <https://doi.org/10.1023/B:SPAC.0000032718.47512.92>

- Nielsen, E., Fraenz, M., Zou, H., Wang, J.-S., Gurnett, D. A., Kirchner, D. L., et al. (2007). Local plasma processes and enhanced electron densities in the lower ionosphere in magnetic cusp regions on Mars. *Planetary and Space Science*, *55*, 2164–2172. <https://doi.org/10.1016/j.pss.2007.07.003>
- Nilsson, H., Edberg, N. J. T., Stenberg, G., Barabash, S., Holmström, M., Futaana, Y., et al. (2011). Heavy ion escape from Mars, influence from solar wind conditions and crustal magnetic fields. *Icarus*, *215*, 475–484. <https://doi.org/10.1016/j.icarus.2011.08.003>
- Øieroset, M., Yamauchi, M., Liszka, L., & Hultqvist, B. (1999). Energetic ion outflow from the dayside ionosphere: Categorization, classification, and statistical study. *Journal of Geophysical Research*, *104*(A11), 24,915–24,927. <https://doi.org/10.1029/1999JA900248>
- Onsager, T. G., Kletzing, C. A., Austin, J. B., & MacKiernan, H. (1993). Model of magnetosheath plasma in the magnetosphere: Cusp and mantle particles at low-altitudes. *Geophysical Research Letters*, *20*, 479–482. <https://doi.org/10.1029/93GL00596>
- Oppennoorth, H. J., Dhillon, R. S., Rosenqvist, L., Lester, M., Edberg, N. J. T., Milan, S. E., et al. (2010). Day-side ionospheric conductivities at Mars. *Planetary and Space Science*, *58*, 1139–1151. <https://doi.org/10.1016/j.pss.2010.04.004>
- Poppe, AR., Fatemi, S., Garrick-Bethell, I., Hemingway, D., & Holmström, M. (2016). Solar wind interaction with the Reiner Gamma crustal magnetic anomaly: Connecting source magnetization to surface weathering. *Icarus*, *266*, 261–266. <https://doi.org/10.1016/j.icarus.2015.11.005>
- Rahmati, A., Larson, D. E., Cravens, T. E., Lillis, R. J., Dunn, P. A., Halekas, J. S., et al. (2015). MAVEN insights into oxygen pickup ions at Mars. *Geophysical Research Letters*, *42*, 8870–8876. <https://doi.org/10.1002/2015GL065262>
- Raines, J. M., Gershman, D. J., Slavin, J. A., Zurbuchen, T. H., Korth, H., Anderson, B. J., & Solomon, S. C. (2014). Structure and dynamics of Mercury's magnetospheric cusp: MESSENGER measurements of protons and planetary ions. *Journal of Geophysical Research: Space Physics*, *119*, 6587–6602. <https://doi.org/10.1002/2014JA020120>
- Ramstad, R., Barabash, S., Futaana, Y., Nilsson, H., & Holmström, M. (2016). Effects of the crustal magnetic fields on the Martian atmospheric ion escape rate. *Geophysical Research Letters*, *43*, 10,574–10,579. <https://doi.org/10.1002/2016GL070135>
- Roelof, E. C. (1997). ENA emission from nearly-mirroring magnetospheric ions interacting with the exosphere. *Advances in Space Research*, *20*, 361–66. [https://doi.org/10.1016/S0273-1177\(97\)00692-3](https://doi.org/10.1016/S0273-1177(97)00692-3)
- Roth, I., & Hudson, M. K. (1985). Lower hybrid heating of ionospheric ions due to ion ring distributions in the cusp. *Journal of Geophysical Research*, *90*(A5), 4191–203. <https://doi.org/10.1029/JA090iA05p04191>
- Saito, Y., Nishino, M., Fujimoto, M., Yamamoto, T., Yokota, S., Tsunakawa, H., et al. (2012). Simultaneous observation of the electron acceleration and ion deceleration over lunar magnetic anomalies. *Earth, Planets and Space*, *64*, 83–92. <https://doi.org/10.5047/eps.2011.07.011>
- Soobiah, Y. I. J., Barabash, S., Nilsson, H., Stenberg, G., Lundin, R., Coates, A. J., et al. (2013). Energy distribution asymmetry of electron precipitation signatures at Mars. *Planetary and Space Science*, *76*, 10–27. <https://doi.org/10.1016/j.pss.2012.10.014>
- Soobiah, Y. I. J., Coates, A. J., Linder, D. R., Kataria, D. O., Wittingham, J. D., Frahm, R. A., et al. (2006). Observations of magnetic anomaly signatures in Mars Express ASPERA-3 ELS data. *Icarus*, *182*, 396–405. <https://doi.org/10.1016/j.icarus.2005.10.034>
- Soobiah, Y. I. J., Wild, J. A., Beharrell, M. J., Barabash, S., Lillis, R. J., Mitchell, D. L., et al. (2014). Properties of a large-scale flux rope and current sheet region on the dayside of Mars: MGS MAG/ER and MEX ASPERA-3 ELS observations. *Icarus*, *242*, 297–315. <https://doi.org/10.1016/j.icarus.2014.08.019>
- Vaisberg, O. (2015). Mars atmospheric losses induced by the solar wind: Comparison of observations with models. *Planetary and Space Science*, *119*, 69–91. <https://doi.org/10.1016/j.pss.2015.09.007>
- Vaisberg, O., Artemyev, A., & Avakov, L. (2015). Nonadiabatic ion acceleration at the nightside highlatitude magnetopause: Fine structure of the velocity distribution function. *Advances in Space Research*, *55*, 2840–2850. <https://doi.org/10.1016/j.asr.2015.02.036>
- Wang, X.-D., Barabash, S., Futaana, Y., Grigoriev, A., & Wurz, P. (2014). Influence of Martian crustal magnetic anomalies on the emission of energetic neutral hydrogen atoms. *Journal of Geophysical Research: Space Physics*, *119*, 8600–8609. <https://doi.org/10.1002/2014JA020307>
- Wang, Y.-C., Luhmann, J. G., Fang, X., Leblanc, F., Johnson, R. E., Ma, Y., & Ip, W.-H. (2015). Statistical studies on Mars atmospheric sputtering by precipitating pickup O⁺: Preparation for the MAVEN mission. *Journal of Geophysical Research: Planets*, *120*, 34–50. <https://doi.org/10.1002/2014JE004660>
- Xu, S., Mitchell, D., Liemohn, M., Fang, X., Ma, Y., Luhmann, J., et al. (2017). Martian low-altitude magnetic topology deduced from MAVEN/SWEA observations. *Journal of Geophysical Research: Space Physics*, *122*, 1831–1852. <https://doi.org/10.1002/2016JA023467>
- Yamauchi, M., Futaana, Y., Fedorov, A., Dubinin, E., Lundin, R., Sauvaud, J.-A., et al. (2006). IMF direction derivation from cycloid-like ion distributions observed by Mars Express. *Space Science Review*, *126*(1–4), 239–266. <https://doi.org/10.1007/s11214-006-9090-1>
- Yamauchi, M., Futaana, Y., Fedorov, A., Kallio, E., Frahm, R. A., Lundin, R., et al. (2008). Advanced method to derive the IMF direction near Mars from cycloidal proton distributions. *Planetary and Space Science*, *56*(8), 1145–1154. <https://doi.org/10.1016/j.pss.2008.02.012>